Modeling gas flow velocities in soils induced by variations in surface pressure, heat and moisture dynamics

W. J. Massman[1] and J. M. Frank[1]

[1] USDA Forest Service, Rocky Mountain Research Station, 240 West Prospect Road, Fort Collins, CO 80526

Key Points:

- The efficiency of atmospheric pressure pumping to the transport of trace gases out of soils and snowpacks is strongly model dependent
- Some models suggest that the daily temperature cycle and rapid changes in soil moisture have an unexpectedly large impact on such transport
- Mesoscale atmospheric phenomena often associated with severe weather and the daily cycle of turbulence cause significant advective transport

Corresponding author: W. J. Massman, william.j.massman@usda.gov

Abstract

Changes in atmospheric pressure continuously ventilate soils and snowpacks. This physical process, known as pressure pumping, is a major factor in the exchange fluxes of H_2O, CO_2 and other trace gases between the soil and atmosphere. Thus models of pressure pumping are relevant to many areas of critical importance. This study compares the three principal models used to describe pressure pumping. Beginning with the fundamental physical principles and whether the flow field is compressible or incompressible, these models are categorized as linear parabolic (one model – compressible) or nonlinear hyperbolic (two models – incompressible). Using observed soil surface pressure data, measured vertical profiles of soil permeability and standard linear analysis and numerical methods, this study shows that nonlinear models produce advective velocities that are one to two orders of magnitude greater than those associated with the linear model. Incorporating soil temperature and moisture dynamics made very little difference to the linear model, but a significant difference in the nonlinear models suggesting that advective velocities induced by pressure changes associated with soil heating and moisture dynamics may not always be small enough to ignore. All numerical results are sensitive to the frequency of the pressure forcing, which was band-pass filtered into low, mid and high frequencies with the greatest model differences at low frequencies. Partitioning the pressure forcing and model responses helped to establish that mid-frequency weather-related phenomena (empirically identified as inertia gravity waves and solitons) are important drivers of gas exchange between the soil and the atmosphere.

Plain Language Summary

Atmospheric pressure is constantly moving air in, out and through the surface of the soil or a snowpack. This pressure pumping (or ventilating) mechanism influences soil water evaporation and snow sublimation, the fluxes of key climate-warming greenhouse gases, and rate at which contaminants can be removed from soils. Thus the ability to model the movement of these gases through these two media is relevant to many current environmental concerns. The present study discusses the differences between the two broad categories of pressure pumping models and points out that these models predict very different ventilation rates. So different that it may be possible to conclude (incorrectly) that the daily cycle for pressure is not significant to soil or snowpack gas exchange. These two model types also respond differently when pressure changes are influenced by changes in soil temperature and moisture, with one type suggesting that dynamic soil temperature and moisture effects are small, in agreement with expectations, and the other suggesting that they can cause surprisingly large effects. Present results also identify (for the first time) specific meso-scale atmospheric waves, often associated with frontal systems, convective activity and rain, can be significant drivers of pressure induced gas exchange.

1 Introduction

For nearly the past 120 years variations in atmospheric pressure and wind at the earth's (solid) surface have been understood as a key mechanism responsible for air movement in and out of soils (Buckingham, 1904) and snowpacks (Dubrovin, 1961). For nearly as long variations of these atmospheric variables have formed the basis for modeling the induced advective velocities within soils (Buckingham, 1904) and snowpacks (Clarke et al., 1987). This phenomenon is often identified as "pressure pumping", "barometric pumping" or "windpumping". (Note: The term pressure pumping will be used exclusively in the present study.) Thus this study focuses advective currents in soils that are driven by periodic (mechanically forced or thermally induced) pressure variations that are distinct from density or thermally driven (i.e., overturning) convective currents that often

dominate fractured or high permeability soils (e.g., Falta et al. (1989); Weisbrod et al. (2009); Nachshon et al. (2012))

Understanding and modeling this phenomenon are important because such air currents can influence key physical and biological processes in the soil and snowpacks through their ability to modify concentration profiles and advective fluxes of gases within and through the pore spaces of these permeable media. For example, these air current transport O_2 (Scotter et al. (1967); Elberling et al. (1998)), CO_2 through both soils (Lewicki et al. (2003); Reicosky et al. (2008); Maier et al. (2012); Laemmel et al. (2017); Moya et al. (2019)) and snowpacks (Bowling and Massman (2011); Berryman et al. (2018); and the video postcard Massman et al. (2021)), water vapor (Fukuda (1955); Scotter and Raats (1969)), CH_4 (Shurpali et al. (1993); Czepiel et al. (2003); Xu et al. (2014); Forde et al. (2019)), N_2O (Massman et al., 1997), gaseous radioactive contaminants (Bourret et al., 2018), Hg vapor (Faïn et al., 2013), isotopes of Rn (Clements and Wilkening (1974); Chen et al. (1995); Robinson et al. (1997); Hu et al. (2018)) and He (Hinkle, 1994). Furthermore, this transport mechanism influences the rate of evaporation of soil water (Ishihara et al., 1992), the sublimation rate of snowpacks (Albert (2002); Drake et al. (2019)), and the volitalization rates and fate of soil contaminants, such as jet fuel (Ostendorf et al., 2000) or other soil contaminants (Forde et al., 2019). In addition, knowledge of the advective velocities induced by pressure pumping may help improve the long term measurements of ecosystem CO_2 fluxes and carbon balance (Massman & Lee, 2002), the formulation of the soil surface boundary condition for land surface (soil-plant-atmosphere) models (e.g., Grifoll et al. (2005)), the fluxes of soil-generated greenhouse gases for climate studies (e.g., Todd-Brown et al. (2012); Rains et al. (2016)), and the transport and deposition of combustion products into the soil during prescribed fires (Massman et al., 2010). The fact that pressure pumping is an important and significant mode of the exchange between the vadose zone and the atmosphere (e.g., Etiope and Martinelli (2002); Rutten (2015)) leads directly to one of the intentions of the present study, which is to expand the research horizons in the area. Nevertheless, this is not necessarily straightforward for three reasons.

First, there are three models describing pressure pumping. The principal difference between them arises when assuming that the flow field is either compressible or incompressible, which in turn leads to estimates of the vertical advective velocity at the soil surface that differ by one or more orders of magnitude, even with identical forcing and soil structure. This difference is significant enough that pointing it out and quantifying it as much as possible is the first intention of the present study. The range and number of settings for interactions between the atmosphere and the earth's surface that involve pressure pumping (e.g., Kuang et al. (2013)) more than justifies a careful look at the differences between these three models.

Second, beyond the mechanical forcing of soil by fluctuations in atmospheric pressure at the soil surface, surface heating can force temperature variations within permeable media and thereby also induce advective flows in both soil (e.g., Kimball (1983); Hinkle (1994); Parlange et al. (1998); Novak (2016)) and snowpacks (e.g., Gray and Morland (1994); Massman et al. (1997); Bartelt et al. (2004)). This is easily understood from the ideal gas law. Whenever the gas temperature within the gas-filled portion of a pore volume changes so also must the pore air pressure (i.e., $\partial p/\partial t \propto \partial T/\partial t$, assuming that the gas filled pore volume is constant), which by Darcy's law will produce an advective flow. But within soils the gas-filled pore volume can change whenever soil water changes phase, i.e., during evaporation or condensation, and during rainfall or irrigation and the concomitant movement of water through the soil matrix. These temperature and moisture influences on induced advective flows have been considered by a few authors, e.g., Kimball (1983); Parlange et al. (1998); Jury and Horton (2004) and Novak (2016) all explore possible temperature effects and Lebeau and Konrad (2009) include the possibility of dynamic changes in soil moisture as part of their modeling study. But it is ex-

pected that temperature and moisture effects are likely to be very small compared to direct pressure effects e.g., Kimball (1983); Massman et al. (1997); Novak (2016)). Nonetheless, (Jury & Horton, 2004, p. 207) do suggest that "Thermally induced convection [authors: 'advection'] is a topic in need of further evaluation", which is the second intent of the present study.

Third, atmospheric pressure at the earth's surface is extraordinarily dynamic and complex, occurring on a variety of scales ranging from weather related high and low pressure systems (the low frequency synoptic scale), through the daily and sub-daily cycles caused by tidal forces and the shorter and more localized mesoscale events (thunderstorms, squall lines, downslope windstorms) to the scale of turbulence (with a time scale on the order of 1-100 seconds or so and a spatial scale of a meter or so). Although these meteorological phenomena are easily identified and often have well characterized barometric pressure signals associated with them, any observed pressure signal will also include common phenomena, which to the authors' knowledge have not been discussed in relation to their forcing of advective flows in soils. Such phenomena include atmospheric infrasound (e.g., Bedard (1998, 2005); Leventhall (2007); Raspet et al. (2019)), high frequency gravity waves (e.g., Marlton et al. (2019); X. Wang et al. (2020)) and other high frequency atmospheric coherent structures (e.g., Einaudi et al. (1989)), lower frequency inertia-gravity waves and other mesoscale scale gravity waves (e.g., Grivet-Talocia et al. (1999); Koch and Siedlarz (1999); Ralph et al. (1999); Koppel et al. (2000); Ruppert and Bosart (2014)), density currents, atmospheric bores and solitons or solitary waves (e.g., Shreffler and Binkowski (1981); Goncharov and Matveyev (1982); Doviak and Ge (1984); Christie (1989); Hauf et al. (1996)). Finally, any measured soil surface pressure signal could also include components unique to a specific location when wind interacts with vegetation (e.g., Finnigan (1979); Shaw et al. (1990); H. Wang and Takle (1995); Nieveen et al. (2001)). The final purpose of the present study is to point out that (what appear in the data to be) inertia-gravity waves and solitons can induce significant advective flows in soils.

The remainder of this study consists four sections. The following section outlines the basic physical and modeling fundamentals and includes an order of magnitude calculation for the advective velocities associated with the different physical processes and models. This second section also develops a semi-observationally based approach for estimating advective velocities in-situ in the hope of better understanding the differences in modeled advective velocities. The third section discusses the experimental site, Manitou Experimental Forest or MEF, and the associated pressure and soil data used with the models. The fourth section presents the results and discussion in terms of three frequency bands for the pressure forcing. Filtering the pressure signal into low (periods $\geq$ 5 hours), mid (periods between 0.5 and 5 hours) and high (periods $\leq$ 0.5 hrs) frequencies helps illuminate the significance impact that inertia-gravity waves and solitons (or more generally, organized mid frequency atmospheric phenomena) can have on pressure pumping in soils. The final section is the summary and conclusion.

2 Physical Fundamentals of Pressure Pumping

Darcy's law and the conservation of mass of soil air (or the equation of continuity of pore air) are foundational elements to developing a model of induced advective flows in soils (e.g., Muskat (1937); Nield (1982); Phillips (1991); Scanlon et al. (2002); Novak (2016)). The 3-D versions of Darcy's law and the conservation of mass (in order) are

$$(\eta - \theta)\mathbf{v} = -\frac{k}{\mu}\nabla P_a \tag{1}$$

and

$$\frac{\partial\big((\eta-\theta)\varrho_a\big)}{\partial t}+\nabla\bullet\left(\mathbf{J_a}+(\eta-\theta)\varrho_a\mathbf{v}\right)=S_a \tag{2}$$

where bold variables are 3-D vectors and $\mathbf{v}$ (ms^{-1}) is the velocity field within the soil, k (m^2) is the soil permeability, μ (Pa s) is the dynamic viscosity of soil air, ∇ (m^{-1}) is the spatial gradient operator, P_a (Pa) is the soil air pressure, η ($\mathrm{m}^3\mathrm{m}^{-3}$) is total soil porosity, θ ($\mathrm{m}^3\mathrm{m}^{-3}$) is the soil volumetric moisture content, $(\eta-\theta)$ is, therefore, the air-filled porosity, ϱ_a (mol m^{-3}) is the molar density of the soil air, t (s) is time, $\mathbf{J_a}$ (mol $\mathrm{m}^{-2}\mathrm{s}^{-1}$) is the diffusional flux of air entering and exiting a soil pore, and S_a (mol $\mathrm{m}^{-3}\mathrm{s}^{-1}$) is the source/sink term of the production/destruction of pore air within the soil.

Because the focus here is on the primary mechanisms causing advective flows the molar diffusive flux, $\mathbf{J_a}$, will not be considered. Further, the source term, S_a, can be eliminated from Equation (2) without sacrificing the influence that changes in θ can have on $\mathbf{v}$ (e.g., Parlange et al. (1998); Lebeau and Konrad (2009); Novak (2016)). In the present context, S_a would only be used to describe soil biochemical reactions involving soil CO_2, O_2 and various nitrogen species, which would have virtually no effect on the air-filled pore volume or $\mathbf{v}$. After these simplifications the ideal gas law is combined with Equation (2); where the ideal gas law is $P_a=\varrho_a R T_K$ and $R=8.314$ $\mathrm{Jmol}^{-1}\mathrm{K}^{-1}$ is the universal gas constant and T_K (K) is the temperature of both the soil air and the soil matrix, which are assumed to be in thermal equilibrium. The resulting equation forms the basis for two different, but related, purposes. The first is prognostic model development (including an order of magnitude estimate of the terms appearing in the various models) and the second is model diagnostics (i.e., model comparisons). Each of these approaches is taken in turn.

2.1 Prognostic Models and Modeling Methods

For prognostic modeling purposes the following equation follows from employing the ideal gas law with Equation (2)

$$\frac{\partial P_a}{\partial t}+\mathbf{v}\bullet\nabla P_a+P_a\nabla\bullet\mathbf{v}=\frac{P_a}{T_K}\left(\frac{\partial T_K}{\partial t}+\mathbf{v}\bullet\nabla T_K\right)+\frac{P_a}{(\eta-\theta)}\left(\frac{\partial\theta}{\partial t}+\mathbf{v}\bullet\nabla\theta\right) \tag{3}$$

Further model development requires simplifying this last expression to 1-D (vertical only), but first it is important to comment on the compressible flow term, $P_a\nabla\bullet\mathbf{v}$, because assuming that the flow is compressible ($\nabla\bullet\mathbf{v}\neq 0$) leads to a very different model of pressure pumping than assuming that the flow is incompressible ($\nabla\bullet\mathbf{v}=0$).

Many pressure pumping models assume incompressible flow (e.g., Muskat (1937); Albert and McGilvary (1992)), as do models of atmospheric pressure fluctuations at the soil surface (e.g., Kraichnan (1956); Yu et al. (2011)), which eliminates the compressible flow term a priori. This is reasonable because in the absence of shocks compressible flow effects are negligible. Or, stated more precisely, compressible flow effects only become important for Mach numbers > 0.3 (Depcik & Loya, 2012), which is not physically realistic for velocities associated with induced advective flows in soils or snowpacks. On the other hand it is appropriate to keep the compressible flow term when describing propagation of sound through soil (e.g., Phillips (1991)). But it is unclear (at least to these authors) how pressure fluctuations associated with sound waves can have any significant influence on advective motions in soils. Nonetheless, the compressible flow model has been used to describe pressure pumping effects (e.g., Buckingham (1904); Clarke et al. (1987)) so it is appropriate to include in this study.

Decomposing the forcing variables (P_a, T_K, θ) into temporally and spatially invariant background components and components that vary with time and spatial dimension, the 1-D form of Equation (3) is

$$\frac{\partial p_\beta}{\partial t} + v\frac{\partial p_\beta}{\partial z} + \left(P + p_\beta\right)\frac{\partial v}{\partial z} = \frac{P}{T_K}\left(\frac{\partial T_\beta}{\partial t} + v\frac{\partial T_\beta}{\partial z}\right) + \frac{P}{(\eta-\theta)}\left(\frac{\partial \theta_\beta}{\partial t} + v\frac{\partial \theta_\beta}{\partial z}\right) \tag{4}$$

where z (m) is the soil depth, v is the induced advective velocity in the vertical direction, the β-subscripted variables ($p_\beta = p_\beta(z,t)$ (Pa); $T_\beta = T_\beta(z,t)$ (C); $\theta_\beta = \theta_\beta(z,t)$ ($\mathrm{m^3 m^{-3}}$)) are the temporally and spatially varying components of P_a, T_K and θ, and P is the time and spatially invariant component of P_a (i.e., $P_a = P + p_\beta$). In general $P \gg p_\beta$ so P substitutes for P_a on the right hand side of Equation (4). But not so on the left hand side because the term $p_\beta \partial v/\partial z$, although relatively small, is relevant and important to the approximate model of pressure pumping in soils discussed below. Also note that the temporally and spatially invariant background components of T_K and θ are not explicitly used as modeling variables.

2.1.1 Three models of advective flows: Pressure forcing only

Traditionally "pressure pumping" models ignore the temperature and soil moisture terms on the right hand side of Equation (4). Including the T_K and θ terms in the three models developed in this section is deferred until the next section, section 2.1.2.

The first model of pressure-only induced advective flows discussed in this section is the Linear (Buckingham, 1904, Appendix A), or Compressible Flow model, the full expression of which follows immediately from Equation (4) and is given as

$$\frac{\partial p_\beta}{\partial t} + v\frac{\partial p_\beta}{\partial z} + (P + p_\beta)\frac{\partial v}{\partial z} = 0 \tag{5}$$

or when combined with Darcy's law is

$$\frac{\partial p_\beta}{\partial t} - \frac{\partial}{\partial z}\left(\kappa\frac{\partial p_\beta}{\partial z}\right) - \frac{\kappa}{P}\left(\frac{\partial p_\beta}{\partial z}\right)^2 - \frac{p_\beta}{P}\frac{\partial}{\partial z}\left(\kappa\frac{\partial p_\beta}{\partial z}\right) = 0 \tag{6}$$

where $\kappa = Pk/((\eta-\theta)\mu)$ ($\mathrm{m^2 s^{-1}}$) is the "pressure diffusivity" (and Darcy's Law is expressed as $v = -(\kappa/P)\partial p_\beta/dz$). The difference between this last expression and Buckingham's original model is that his model includes only the first term on the left hand side and not the second or third terms, both of which are quite small relative to first term. It is easy to see that the third term on the left can be ignored relative to the first, because if follows immediately from $p_\beta \ll P$ or equivalently $p_\beta/P \ll 1$. Showing that the second term on the left is small relative to the first term, i.e., $\kappa/P\left(\partial p_\beta/\partial z\right)^2 \ll \partial/\partial z\left(\kappa\partial p_\beta/\partial z\right)$ is somewhat more involved and so is left for Section 2.2.1. Therefore, the Linear model (Buckingham, 1904), which is given next, should be accurate to a high degree of numerical precision.

$$\frac{\partial p_\beta}{\partial t} - \frac{\partial}{\partial z}\left(\kappa\frac{\partial p_\beta}{\partial z}\right) = 0 \quad \text{Linear model} \tag{7}$$

Before proceeding to the second model there is an interesting variant to Buckingham's original model, which is

$$\frac{\partial p_\beta}{\partial t} - \frac{\partial}{\partial z}\left(\kappa \frac{\partial p_\beta}{\partial z}\right) - \frac{\kappa}{P}\left(\frac{\partial p_\beta}{\partial z}\right)^2 = 0 \tag{8}$$

which follows by dropping the third term of Equation (6) (because as shown in section 2.1.2, $\left(p_\beta/P\right)\partial/\partial z\left(\kappa \partial p_\beta/\partial z\right) \ll \kappa/P\left(\partial p_\beta/\partial z\right)^2$). Unlike Buckingham's original model, which is linear and parabolic, this equation is weakly non-linear, although still parabolic because as discussed above the first term on the right is still much larger than the non-linear second term. This variant of the Linear pressure pumping model is pointed here because, as shown in the Appendix A, Equation (8) can be related to the viscid Burgers Equation and is, therefore, amenable to an analytical solution.

The second model explored here is the Muskat (Muskat, 1937) or Incompressible Flow model, which is given as

$$\frac{\partial p_\beta}{\partial t} + v\frac{\partial p_\beta}{\partial z} = 0 \tag{9}$$

When combined with Darcy's law this yields:

$$\frac{\partial p_\beta}{\partial t} - \frac{k}{(\eta-\theta)\mu}\left(\frac{\partial p_\beta}{\partial z}\right)^2 = 0 \qquad \text{or} \qquad \frac{\partial p_\beta}{\partial t} - \frac{\kappa}{P}\left(\frac{\partial p_\beta}{\partial z}\right)^2 = 0 \quad \text{Muskat model} \tag{10}$$

where the compressible flow term (which is proportional to $\partial v/\partial z$) does not appear in this model. Unlike the Linear model, this model is nonlinear and hyperbolic and, as also shown in Appendix A, can be transformed into the inviscid Burgers Equation. Although this identity with the Burgers Equation is not employed in this study, it is worth pointing out because this may offer other insights into solution methods for Equation (10).

The third model of pressure pumping is an approximation to the Muskat model that originated with Kidder (1957) (crediting Muskat (1937)) and further developed by J. W. Massmann (1989). It is obtained by adding $-(\kappa/P)\, p_\beta\left(\partial^2 p_\beta/\partial z^2\right)$ to the left hand side (of the second expression) of Equation (10) and then employing the identity $(\partial p_\beta/\partial z)^2 + p_\beta\left(\partial^2 p_\beta/\partial z^2\right) = \partial^2(p_\beta^2/2)/\partial z^2$ to yield the Kidder model, or the Approximate Incompressible Flow model:

$$\frac{\partial p_\beta}{\partial t} - \left(\frac{\kappa}{P}\right)\frac{\partial^2(p_\beta^2/2)}{\partial z^2} = 0 \quad \text{Approximate model} \tag{11}$$

This model is only justifiable because the term, $p_\beta\left(\partial^2 p_\beta/\partial z^2\right)$ is quite small relative to the original nonlinear term, $(\partial p_\beta/\partial z)^2$, an inequality that was discussed above and is proven in section 2.2.1. Although the Kidder model may appear to be a nonlinear parabolic equation, it remains a nonlinear hyperbolic equation. Interestingly though, the Approximate model may offer some computational benefit over the Muskat model because it was often more stable numerically than the Muskat model – likely because of the addition of a weak, albeit non-linear, diffusive term (e.g., Thomas (1995, Section 5.3.3)).

In summary, the three models examined in this study are Equation (7) (the Linear or Compressible Flow model), Equation (10) (the Muskat or Incompressible Flow model) and Equation (11) (the Kidder or the Approximate Incompressible Flow model) and, as demonstrated in Section 4, there are some significant differences in the predictions of $v(t,z)$

and (especially) $v(t,0)$ that are associated with these three models. But before ending this section, it may be worth a brief discussion of the model first proposed by Shan (1995) and further developed by Scanlon et al. (2002) and later employed by J. Li et al. (2011) and (especially) J. Li et al. (2012).

The Quasi-Linear model (Shan (1995); Scanlon et al. (2002)) is

$$\frac{\partial P_a^2}{\partial t} - \kappa \frac{\partial^2 P_a^2}{\partial z^2} = 0 \qquad \text{Quasi-Linear model} \tag{12}$$

Except for a change of notation this last equation is identical to Equation (1) of Shan (1995) and Equation (8.30) of Scanlon et al. (2002). But Scanlon et al. (2002) show that the Quasi-linear model can be linearized to yield what is essentially the Compressible Flow model, Equation (7) above (see Equation (8.31) of Scanlon et al. (2002)). But the Compressible Flow model can only be derived by assuming the flow is compressible. It is by its nature predominantly linear (as shown previously) and it is not a consequence of the linearization of a nonlinear model. Therefore, the Quasi-Linear model is completely unnecessary. But more importantly, combining either Equation (8.30) of Scanlon et al. (2002) or equivalently Equation (12) with the incompressible flow assumption does not and cannot logically lead to Equation (8.31) of Scanlon et al. (2002) (= the Compressible Flow model). Therefore, models based on the Quasi-Linear model, Equation (12) above, are at the very least unnecessary and may in fact be completely wrong, especially if it is thought of as a further refinement of the Approximate Incompressible Flow model (Equation (11) above). Confusing Equation (12) as a variant of Equation (11) might lead to substituting p_β for P_a in Equation (12) above (i.e., replacing Equation (12) with $\partial p_\beta^2/\partial t - \kappa \partial^2 p_\beta^2/\partial z^2 = 0$). This last equation for p_β^2 cannot be logically justified on the basis of being related to the Approximate model. Regardless of the assumption made concerning the flow, simply recognizing that the Approximate model is valid is sufficient to show that the equation $\partial p_\beta^2/\partial t - \kappa \partial^2 p_\beta^2/\partial z^2 = 0$ violates the physically valid assumption that $p_\beta \ll P$.

2.1.2 Three models of advective flows: Including T_K and θ forcing

Each of the three models discussed above can be generalized to include the influence that changes in soil temperature and moisture can have on $p_\beta = p_\beta(t,z)$ and $v = v(t,z)$. These generalizations are (in the order as above)

$$\frac{\partial p_\beta}{\partial t} - \frac{\partial}{\partial z}\left(\kappa \frac{\partial p_\beta}{\partial z}\right) + \Lambda_z \frac{\kappa}{P}\left(\frac{\partial p_\beta}{\partial z}\right) = \Lambda_t \qquad \text{Linear model} \tag{13}$$

$$\frac{\partial p_\beta}{\partial t} - \frac{\kappa}{P}\left(\frac{\partial p_\beta}{\partial z}\right)^2 + \Lambda_z \frac{\kappa}{P}\left(\frac{\partial p_\beta}{\partial z}\right) = \Lambda_t \qquad \text{Muskat model} \tag{14}$$

$$\frac{\partial p_\beta}{\partial t} - \frac{\kappa}{P}\left(\frac{\partial^2 (p_\beta^2/2)}{\partial z^2}\right) + \Lambda_z \frac{\kappa}{P}\left(\frac{\partial p_\beta}{\partial z}\right) = \Lambda_t \qquad \text{Approximate model} \tag{15}$$

where Λ_t (Pa s^{-1}) $= \Lambda_t(t,z) = (P/T_K)\partial T_\beta/\partial t + (P/(\eta-\theta))\partial\theta_\beta/\partial t$ and Λ_z (Pa m^{-1}) $= \Lambda_z(t.z) = (P/T_K)\partial T_\beta/\partial z + (P/(\eta-\theta))\partial\theta_\beta/\partial z$.

To keep the modeling and numerical methods as simple and as realistic as possible $\Lambda_t(t,z)$ and $\Lambda_z(t,z)$ are input as external analytical expressions obtained by differentiating analytical expressions for $T_\beta(t,z)$ and $\theta_\beta(t,z)$, which are obtained by curve-

fitting the observed soil surface temperature, $T_\beta(t,0)$, and the 0.02 m depth soil moisture, $\theta_\beta(t, z = 0.02\,\mathrm{m})$. Here I assume that $\theta_\beta(t,0) \approx \theta_\beta(t, z = 0.02\,\mathrm{m})$, which is not unreasonable for the present study because it is focused on a very dry semiarid site that does not display strong moisture dynamics.

$T_\beta(t,0)$ is approximated analytically as $\Sigma_i F_{Ti}(t,0)$, where $F_{Ti}(t,0) = \Delta T_{\beta i} \sin(\omega_i t + \phi_i)$ is the predominant functional form, but can be other functions necessary to capture low and mid-frequency transients associated with synoptic scale weather systems or clouds. Given an analytical expression for $T_\beta(t,0)$, then $T_\beta(t,z) = \Sigma_i F_{Ti}(t,z)\exp(-z/D_{Ti})$, where $F_{Ti}(t,z) = \Delta T_{\beta i} \sin(\omega_i t + \phi_i - z/D_{Ti})$ and D_{Ti} is estimated by scaling the temperature attenuation depth associated with the diel cycle, D_T (where D_T was determined from the observed temperature profiles to be 0.12 m during June 2012 and 0.14 m during October 2012), to ω_i (or other non-sinusoidal frequency-like parameters). The sampling frequency for the soil surface temperature (5 minutes) and the sensitivity of the soil temperature probe largely eliminated any possibility of obtaining any high frequency temperature data information for the present study. Consequently, the only frequency content in the temperature data are the low and mid frequencies.

A similar method is employed for the soil moisture at 0.02 m, i.e., $\theta_\beta(t, z = 0.02\,\mathrm{m}) = \Sigma_i F_{\theta_i}(t,0)$. The set of functions $F_{\theta_i}(t,0)$ are largely specific to a given observation period and are not necessarily sinusoidal in time to allow for those occasions when rain may rapidly increase soil moisture or the soil moisture decreases with drying or drainage. The attenuation depths for soil moisture variations were modeled in a manner similar to temperature, but inferred from the moisture observations. But precision estimates in the attenuation depths for soil moisture are not critical to the model simulations because the soil was extremely dry during the observation periods and most soil moisture dynamics were confined to the upper few centimeters of soil, except for the overall drying trend in soil moisture, which did extend to nearly a meter in depth. But because of the nature of the data and the sensitivity of the soil moisture probe $\theta_\beta(t,z)$ contains only low frequency information. Finally, because soil moisture at this site was generally less that 0.15 $\mathrm{m^3 m^{-3}}$ at all times there is no concern about a saturated soil, i.e., $(\eta - \theta) \rightarrow 0$ in the denominator of either $\Lambda_t(t,z)$ and $\Lambda_z(t,z)$.

The initial conditions for temperature and moisture, $T_K(0,z)$ and $\theta(0,z)$, are obtained by curve fitting their observed profiles at the start of the simulation.

2.1.3 Numerical methods, Initial conditions and Boundary conditions

The Linear models, Equations (7) and (13), are solved numerically using an implicit Crank-Nicolson scheme followed by three iterations of a Newton-Raphson solver to refine the Crank-Nicolson solution. Three iterations of the Newton-Raphson solver were sufficient to produce a convergence $< 10^{-10}$ Pa. The nonlinear models, Equations (10) and (14) for the Muskat model and Equations (11) and (15) for the Approximate model, are solved with an implicit finite difference scheme adapted after Lax-Friedrichs method (e.g., Thomas (1995, p. 215); Press et al. (2007, p. 1034); Kurganov (2016, Eqn. (26)); Hinch (2020, Chapter 10)), which is followed by three iterations of the Newton-Raphson solver again achieving a convergence $< 10^{-10}$ Pa. The Newton-Raphson step is intended to reduce numerical errors in the solution for $p_\beta(t,z)$ and thereby improve stability of the Lax-Friedrichs scheme for the hyperbolic models. It was of less benefit to the Crank-Nicolson scheme and the Linear models.

But because the nonlinear hyperbolic models discussed here, i.e, Equations (10) and (11), do not quite fit the archetypal Lax-Friedrichs schemes discussed in the references above it is worthwhile to briefly discuss the numerical method used here. The most fundamental expression of which is the following:

$$\widetilde{p}_i^{j+1} - \left(\frac{\Delta t}{4\Delta z^2}\frac{\kappa_i}{P}\right)\left(\widetilde{p}_{i+1}^{j+1} - \widetilde{p}_{i-1}^{j+1}\right)^2 = \frac{1}{2}\left(\widetilde{p}_{i+1}^{j} + \widetilde{p}_{i-1}^{j}\right)$$

where $i = 1, 2, \cdots, M$ refers to the spatial discretization index (with M layers) and j is the time step index. In terms of the Newton-Raphson function to be minimized at the $j+1$ time step, i.e., $\widetilde{\mathcal{P}}_i = \widetilde{\mathcal{P}}_i(\widetilde{p}_{i-1}^{j+1}, \widetilde{p}_i^{j+1}, \widetilde{p}_{i+1}^{j+1})$, this yields:

$$\widetilde{\mathcal{P}}_i = \widetilde{p}_i^{j+1} - \frac{r_i}{4}\left(\widetilde{p}_{i+1}^{j+1} - \widetilde{p}_{i-1}^{j+1}\right)^2 - \frac{1}{2}\left(\widetilde{p}_{i+1}^{j} + \widetilde{p}_{i-1}^{j}\right)$$

where $r_i = \Delta t\,\kappa_i/(\Delta z^2 P)$ $\left(\mathrm{Pa}^{-1}\right)$ and this numerical scheme, appropriate to the Muskat model, is easily generalized to the Approximate model and the models that include temperature and moisture dynamics. Although this Lax-Friedrichs-Newton-Raphson numerical scheme does appear to yield quite plausible and physically realistic solutions, it was not the only numerical scheme investigated. The explicit Lax-Friedrichs method and both the explicit and implicit Lax-Wendroth (with a Newton-Raphson solver for the implicit approach) were also investigated and compared. The present scheme seems to be the most reliable of all those tested. Possible contributing factors to the performance of the present numerical scheme is that the velocity field being modeled is unlikely to develop shocks, nor are there any discontinuities in the input data that are sufficient to promote their formation.

The initial condition for pressure cannot be determined directly from observations. Therefore, the present study assumes that $p_\beta(0,z) = p_\beta(0,0)(1-\epsilon+\epsilon\exp(-z/D_{p,init}))$, where $p_\beta(0,0)$ is the observed surface pressure perturbation at $t = 0$, $\epsilon = 0.08$ and $D_{p,init} = 60$ m. This parameterization is somewhat arbitrary, but it is reasonable and it provides a simple continuous function for the model's initial conditions. Furthermore, since the purpose of the present study is to compare different model estimates of $v(t,z)$ and especially $v(t,0)$ the key consideration here is not whether the models are sensitive to the initial conditions, but that the initial conditions are the same for each model run. Nonetheless, a sensitivity analysis was performed to examine the model's sensitivity to ϵ and $D_{p,init}$ by first comparing $\epsilon = 0$ (uniform initial pressure field) with that assuming $\epsilon = 0.08$. The difference in the Linear and Muskat model all frequencies solutions near the surface, $v(t,0)$, were usually quite small $< 0.1\%$. The differences could be larger at greater depths because the permeability at this site increases by a couple orders of magnitude within the upper 0.5 m of soil, but again not significantly so. Similar conclusions were reached when varying $D_{p,init}$, except for the Muskat model for low frequencies, for which the difference was $< 6\%$. In general, the initial conditions should not be viewed as a source of significant concern in the preset study.

The lower bound of the spatial domain is 20 m (below the soil surface) and the grid spacing is 0.10 m for all models. The lower boundary condition (LBC) is $\partial^2 p_\beta/\partial z^2 = 0$, i.e., a "pass-through" boundary condition. But because the soil permeability was set to a very low value ($k \le 10^{-15}$ m^2) in the lowest third of the domain (a region of the soil for which there is no permeability data), the solution is not very sensitive to the specifics of the LBC. This constraint on k also helped improve stability of the numerical solution of the nonlinear models. The upper boundary condition is obtained from differential pressure measurements made on the soil surface and sampled at once per second (1 Hz). The 1 Hz pressure time series was decomposed using a Savitzky-Golay filter (e.g., Press et al. (2007, p. 766)) into a low frequency component (pressure signals with periods ≥ 5 hours), a mid-range frequency component (pressure signals with periods between 0.5 and 5 hours) and high frequency component (with periods between 1 s and 0.5 hours). Each of these component time series is used separately for the upper boundary condition. To minimize potential numerical instabilities, particularly for the Muskat model, the time step is set to 1 second, i.e., the upper boundary condition is the observed or filtered 1

Hz pressure data. Likewise, the analytical expressions for $\Lambda_t(t,z)$ and $\Lambda_t(t,z)$ are input at 1 second intervals. All model coding was done in MatLab version 2019b.

2.2 Preliminary Model Diagnostics

2.2.1 A Numerical Example: Advective Velocities and Soil Evaporation

Because much of this study is devoted to comparing magnitudes of different estimates of the advective velocity this section provides some context for these estimates using soil evaporation as an example. But, it is also important to emphasize that soil evaporation is just one of many possible examples, so this particular case is not necessarily indicative of the significance of advective transport of any other trace gas in soil or other permeable media or for other environmental settings.

The advective flux of water vapor from the soil is $\rho_v v$ ($\mathrm{kgm^{-2}s^{-1}}$), where ρ_v ($\mathrm{kgm^{-3}}$) is the mass density of the advected soil vapor and v ($\mathrm{ms^{-1}}$) is the (vertical) advection velocity. To aid in the interpretation of the mass fluxes this evaporative flux is expressed in terms of energy units, i.e., the flux is $L_v\rho_v v$; where L_v is the enthalpy of vaporization of water $\approx 2.5\times10^6$ $\mathrm{Jkg^{-1}}$. Assuming that the soil temperature is between 10 C and 30 C and that the soil vapor is saturated, it follows that ρ_v is between 0.01 and 0.03 $\mathrm{kgm^{-3}}$. Next allowing v to be between 1 and 1000 $\mu\mathrm{ms^{-1}}$ (values that will be discussed and justified in the next and later sections), it follows that evaporative energy flux (density) should be between about 0.025 $\mathrm{Wm^{-2}}$ and 75 $\mathrm{Wm^{-2}}$. Or to put it another way, assuming any advective flux that contributes more than approximately 5 $\mathrm{Wm^{-2}}$ to soil evaporation is significant, then it follows that the advective velocity must exceed a threshold value of ≈ 100 $\mu\mathrm{ms^{-1}}$. For the present purposes, this threshold is fairly crude because it can vary within a factor of two or so. But, it is not unreasonable and it should help with the interpretation of later results.

2.2.2 Linear Analysis: Magnitudes of advective velocities

This section serves two purposes. The first is to validate the expectations that $\kappa/P\left(\partial p_\beta/\partial z\right)^2 \ll \partial/\partial z\left(\kappa\partial p_\beta/\partial z\right)$ for the Linear model and $p_\beta(\partial^2 p_\beta/\partial z^2) \ll (\partial p_\beta/\partial z)^2$ for the Approximate model. The second is to compare numerical estimates of the advective velocities associated with each of the three pressure-only models to the temperature-only and θ-only models. For brevity and convenience this discussion is limited solely to the diel cycle (i.e., $\omega = 7.272\times10^{-5}$ radians $\mathrm{s^{-1}}$). Nonetheless the numerical results (Section 4) validate the conclusions of this section for the diel cycle and show that the 24-hour cycle is useful surrogate for all low frequencies (here defined with periods ≥ 5 hours). The mid-range and high frequency results are deferred until Section 4 below, as are all results associated with including the temperature and θ effects (i.e., Equations (13), (14) and (15)).

The temperature-only advective velocity, v_T, is estimated from $\partial T_\beta/\partial t = v_T\partial T_\beta/\partial z$; where $\partial T_\beta/\partial t \approx \omega\Delta T_\beta$, $\partial T_\beta/\partial z \approx -\Delta T_\beta/D_T$, ΔT_β (C) is the amplitude of the diel cycle, D_T (m) is the attenuation depth associated with the diel-temperature wave, i.e., 0.07 m $\leq D_T \leq$ 0.14 m and for the sake of simplicity the phase between $\partial T_\beta/\partial t$ and $\partial T_\beta/\partial z$ is not considered in this section (which is the same for the pressure and soil moisture discussions below as well). Therefore,

$$|v_T| = \omega D_T \approx (5-10)\times10^{-6}\ \mathrm{ms^{-1}}$$

where, because the principal concern here is orders of magnitude, the results are presented as absolute values (or equivalently the amplitude) of the induced advective velocities. Luce et al. (2013) use a similar approach to estimate the advective velocity of thermally

induced flow in stream beds. Also relevant here is the estimate of $|v_T|$ that can be derived from Kimball (1983), which is

$$|v_T| \approx (0.1) \times 10^{-6} \text{ ms}^{-1} \quad \text{(Kimball, 1983)}$$

This is roughly two orders of magnitude smaller than the preceding estimate of v_T. This difference will be discussed further in Section 4.

The θ-only advective velocity, v_θ, is estimated from $\partial\theta/\partial t = v_\theta \partial\theta/\partial z$. But estimating $\partial\theta/\partial t$ and $\partial\theta/\partial z$ cannot be determined from a well established theory as was done with v_T. So both terms need to be estimated separately from observations. There are two components to $\partial\theta/\partial t$. The first is the amplitude of a daily cycle ($\Delta\theta_\beta$) and the other is a more-or-less decreasing linear trend. $\Delta\theta_\beta$ can be estimated from Rose (1968); R. D. Jackson (1973); T. J. Jackson et al. (1997); Brooks et al. (2002); Novak (2016) and the MEF data used in this study and presented later. This yields $\Delta\theta_\beta = 0.02$ m^3m^{-3} (varying between 0 to 0.025 m^3m^{-3}), which suggests that $\omega\Delta\theta_\beta \approx 1.4 \times 10^{-6}$ s^{-1}. Novak (2016) estimates a maximum magnitude of the (decreasing) linear trend (i.e., a drying soil) to be θ to be -1.2×10^{-7} s^{-1}. The MEF data used in the present study suggest a similar value for a drying soil, but the same data also suggest that for a wetting soil $|\partial\theta/\partial t| > 1.4 \times 10^{-6}$ s^{-1}. Finally, the other data sources above suggest that for this decreasing linear trend $|\partial\theta/\partial t| < 10^{-8}$ s^{-1} is also possible. Estimating a daily value of $\partial\theta/\partial z$ from these same data sources yields a value of $\partial\theta/\partial z$ of about 0.33 m^{-1} (varying between 0 to 0.4 m^{-1}). To keep the estimate of v_θ reasonable only $\partial\theta/\partial z = 0.33$ m^{-1} is considered. Note that the data for some of these numerical estimates may not have included the temperature corrections appropriate to TDR measurements of volumetric soil moisture (e.g., Or and Wraith (2000); Massman et al. (2010, Appendix A)). We found that these corrections did not introduce any significant differences into the order of magnitude estimate of v_θ below or the conclusions drawn from them.

Synthesizing these results suggest

$$|v_\theta| = \frac{|\partial\theta/\partial t|}{|\partial\theta/\partial z|} \approx \frac{(0-1.6)10^{-6}}{0.33} \approx (0-5) \times 10^{-6} \text{ ms}^{-1}$$

This estimate of $|v_\theta|$, and especially the relatively larger values, are extremely uncertain (and potentially unreliable), largely because of the need to divide by $\partial\theta/\partial z$, which spans a very wide range including values approaching zero. The realism of the high end estimates of v_θ will be reexamined in Section 4.

Comparing these estimates of $|v_T|$ and $|v_\theta|$ suggest that $|v_\theta| < |v_T|$ is likely and, given the uncertainty inherent in v_θ, $|v_\theta| \ll |v_T|$ is nearly as likely. But in general when the soil is warming ($\partial T_\beta/\partial t > 0$) the soil dries out through evaporation, which results in $\partial\theta_\beta/\partial t < 0$. Therefore, v_θ will likely be (at least partially) out of phase with v_T and therefore, will reduce the effective v_T. So it is also reasonable to expect that $|v_\theta| < |v_T + v_\theta| \leq |v_T|$.

The pressure-only advective velocity is complicated by the need to examine three different models. For the Linear model to be valid it is necessary to show that the incompressible term ($v_p \partial p_\beta/\partial z$) is much smaller than the compressible term ($P\,\partial v_p/\partial z$) for the following approximation to Equation (5) (i.e., $\partial p_\beta/\partial t = v_p \partial p_\beta/\partial z + P\,\partial v_p/\partial z$); where the '$p$' subscript ($v_p$) refers to the pressure-induced velocity. Here I assume that both p_β and v_p attenuate with depth according to $\exp(-z/D_p)$, where D_p (m) is the pressure attenuation depth and that both are periodic in time, $\sin(\omega t)$. Therefore, analogous to T_β and v_T above, $\partial p_\beta/\partial t \sim \omega\Delta p_\beta$, $v_p \partial p_\beta/\partial z \sim v_p \Delta p_\beta/D_p$ and $P\,\partial v_p/\partial z \sim P v_p/D_p$; where Δp_β is the amplitude of the pressure "wave" at the soil surface. From $\Delta p_\beta \ll P$ it follows that the incompressible term is much smaller than the compressible term

and the Linear model is valid. Therefore $v_{pL} = \omega D_p \Delta p_\beta / P$, where the '$L$' subscript refers to 'Linear model'. It is possible to estimate D_p from the linear theory of pressure pumping: i.e., $D_p = \sqrt{2\kappa/\omega}$ (e.g., Waddington et al. (1995)). Assuming a soil permeability (k) between 10^{-10} and 10^{-12} m^2, $\Delta p_\beta \sim 100$ Pa, $P = 10^5$ Pa, $\mu = 1.85\times10^{-5}$ Pa s and $\eta - \theta \sim 0.4$, yields $\kappa = 0.0125 - 1.25$ m^{2}s^{-1}, $D_p \sim 16 - 180$ m and the following order of magnitude estimate of $|v_{pL}|$

$$|v_{pL}| = \omega D_p \frac{\Delta p_\beta}{P} = \left(\sqrt{2\kappa\omega}\right) \frac{\Delta p_\beta}{P} = (1 - 10) \times 10^{-6} \text{ ms}^{-1}$$

The range of values for $10^{-12} \leq k \leq 10^{-10}$ is representative of the soil permeability at Manitou Experimental Forest (see Appendix B) and the assignment of a value of 100 Pa to Δp_β provides a reasonable estimate of the combined amplitudes of diurnal and semi-diurnal tides (e.g., Mass et al. (1991); Y. Li and Smith (2010); Marty et al. (2010)).

Nonetheless, this estimate of $|v_{pL}|$ is clearly sensitive to Δp_β (or to be more precise $\partial p_\beta / \partial t$) and Δp_β can take on a variety of values associated with variety of different low frequency atmospheric phenomena. For example, J. Massmann and Ferrier (1992) use a pressure amplitude of about 2400 Pa (24 mb) and a period of 24 hours for their simulations. Although such large drops in surface pressure are certainly possible, they are extremely rare on a synoptic scale (i.e., during a 24 hour period). Drops in surface pressure at rates $\geq$ 1 mb hr^{-1} or $\geq$ 100 Pa hr^{-1} on the synoptic scale are usually associated with bombogenesis (e.g., Sanders and Gyakum (1980)), i.e, the genesis of Bomb Cyclones and other types of severe weather. Otherwise, they do not characterize normal ambient atmospheric conditions.

Clements and Wilkening (1974) use surface pressure observations that are more typical of synoptic scale frontal passages in their study of advective velocities in soils. They found that $\partial p_\beta / \partial t$ = -65 Pa hr^{-1} and 50 Pa hr^{-1}, which on a 24-hour basis would correspond to $|\Delta p_\beta| \approx 1200 - 1600$ Pa. Further, using $k = 10^{-12}$ m^2 and $P \approx 86$ kPa, Clements and Wilkening (1974) estimate $|v_{pL}| \approx 100 \times 10^{-6}$ ms^{-1}. Given these data it should come as no surprise that Clements and Wilkening (1974) estimate $|v_{pL}|$ exceeds, by at least an order of magnitude, $|v_{pL}|$ given above. But, more importantly though is that Clements and Wilkening's (1974) estimate of $|v_L|$, which is associated with frontal passages, supports the reasonableness of our estimate of $|v_L|$ associated with diel barometric forcing.

The assumption of a depth-attenuated sinusoidal solution underlying the estimates of v_T and v_{pL} works well because it is a valid linear solution to the linear parabolic equations that describe $T_K(t,z)$ and $p_\beta(t,z)$. Such an approach will not necessarily work as well with the Muskat and Approximate models because they are nonlinear hyperbolic equations, for which numerical methods are preferred. Nonetheless, there is some value in adapting this linear approach to these two nonlinear models because it does offer insights into these two nonlinear models, their relationship to one another and how v_p estimated with these two models compare to $|v_T|$, $|v_\theta|$ and $|v_{pL}|$.

Estimating v_p for the Muskat model (i.e., v_{pM}) follows immediately from expressing the Muskat model in terms of velocity, i.e., $\partial p_\beta / \partial t - (P/\kappa) v_{pM}^2 = 0$. Substituting $\omega \Delta p_\beta$ for $\partial p_\beta / \partial t$ and solving for v_{pM} and then the order of magnitude estimate yields

$$|v_{pM}| = \sqrt{\omega \kappa \Delta p_\beta / P} = (30 - 300) \times 10^{-6} \text{ ms}^{-1}$$

This range of values for $|v_{pM}|$ is well supported by their agreement with the estimate of $|v| \sim (28 - 990) \times 10^{-6}$ ms^{-1} derived by Iakovleva and Ryzhakova (2003, Table 2) from soil Radon transport measurements.

The relationship between $|v_{pL}|$ and $|v_{pM}|$ can be made more explicit by taking the ratio of $|v_{pL}|$ to $|v_{pM}|$, which yields

$$\frac{|v_{pL}|}{|v_{pM}|} = \sqrt{2\frac{\Delta p_\beta}{P}} \approx 0.045 \ll 1$$

where the numerical values results from assuming (as above) $\Delta p_\beta \sim 100$ Pa and $P = 10^5$ Pa. This result clearly indicates to expect that $|v_{pL}| <$ or $\ll |v_{pM}|$. But more interestingly, this relationship is not explicitly a function of frequency of the (oscillatory) forcing pressure. Therefore, this linear analysis yields a specific prediction regarding the velocities produced by the Linear and Muskat models, which is that the ratio of the modeled velocities increases with increasing Δp_β. Therefore, because the amplitude of atmospheric pressure perturbations tends to decrease with increasing frequency it follows to expect that $|v_{pL}|/|v_{pM}|$ will be maximal at low frequencies and minimal at high frequencies. This theoretical result will be tested in a later section summarizing the various models' responses to low, mid and high frequency forcing.

For the Approximate model to be valid $\kappa p_\beta / P \partial^2 p_\beta / \partial z^2 \ll (P/\kappa) v_{pM}^2$ must be true or equivalently that $(\kappa \Delta p_\beta / P)(\Delta p_\beta / D_p^2) \ll \omega \Delta p_\beta$. Assuming that D_p from the Linear model is also valid for the Approximate and Muskat (or non-linear) models and substituting the expression for D_p above into D_p^2 results in $(p_\beta/(2P))\omega \Delta p_\beta \ll \omega \Delta p_\beta$, which is obviously true because $p_\beta/(2P) < p_\beta/P \approx 10^{-3} \ll 1$. The order of magnitude estimate of v_{pA} follows by replacing the differential form of the Approximate model with the algebraic form as has been throughout this section. The result is

$$|v_{pA}| = |v_{pM}| \sqrt{1 + 2\Delta p_\beta / P} \approx |v_{pM}| \approx (30 - 300) \times 10^{-6} \text{ ms}^{-1}$$

The key takeaways at this point in the analysis are (1) the approximations necessary to justify the Linear and Approximate models are valid, (2) for low frequency surface forcing (i.e., with periods within a factor of five or so of the daily cycle) the following ordering of the models' advective velocities is:

$$|v_\theta| < |v_T + v_\theta| \leq |v_T| \sim |v_{pL}| \ll |v_{pM}| \approx |v_{pA}| \tag{16}$$

and (3) because $|v_T| \sim |v_{pL}|$ it may not be possible to assume a priori that advective flows associated with temperature dynamics are small relative to those of pressure, especially for low porosity soils, e.g., $k \leq 10^{-14}$ m^2. This supports the need to examine the interactions of temperature and pressure on the advective transport velocity with models based on Equations (13), (14) and (15). To that end, the linear analysis is applied to Equation (13).

This requires replacing the differential equation, $\partial p_\beta / \partial t - \Lambda_t + P \partial v_p / \partial z - \Lambda_z v_p = 0$ with the following algebraic one $\omega \Delta p_\beta - P \omega \Delta T_\beta / T_K = P v_{pL*} / D_p - P \Delta T_\beta / (T_K D_T) v_{pL*}$ and solving for v_{pL*}; where the subscript '$*$' refers to the pressure-induced velocity, v_{pL}, that includes the temperature and moisture terms. But here we consider only the temperature effects on v_{pL} for the sake of simplicity. A bit of mathematical manipulation yields the following:

$$\omega D_p \frac{\Delta p_\beta}{P} \left(1 - \frac{P}{\Delta p_\beta} \frac{\Delta T_\beta}{T_K}\right) = \left(1 - \frac{D_p}{D_T} \frac{\Delta T_\beta}{T_K}\right) v_{pL*}$$

After assuming that $T_K \approx 300$ K and given all other previous estimates above for the other terms in this equation, it is straightforward to show that $(P/\Delta p_\beta)/(\Delta T_\beta / T_K) \gg 1$ and $(D_p/D_T)/(\Delta T_\beta / T_K) \gg 1$, from which it the follows immediately that

$$|v_{pL*}| = \frac{D_T}{D_p}\frac{P}{\Delta p_\beta}|v_{pL}| = \sqrt{\frac{\kappa_T}{\kappa}}\frac{P}{\Delta p_\beta}|v_{pL}| = C_{L*}|v_{pL}| \sim (0.4-9)\times|v_{pL}|$$

where $\kappa_T = (0.1-0.7)\times 10^{-6}$ m^{2}s^{-1} is the soil's thermal diffusivity (e.g., Campbell and Norman (1998, p. 124)) . For the present purposes the principal determinant of the coefficient C_{L*} is $1/D_p$ or κ, the soil's pressure diffusivity. Meaning that as permeability decreases the temperature (and moisture) effects become increasingly more important, confirming the conclusion of the linear analysis of the individual velocities, $|v_T|$, $|v_\theta|$, and $|v_p|$ above. This last relationship also suggests that in terms of absolute magnitudes, it seems reasonable to conclude that either $|v_{pL*}| \sim |v_{pL}|$ or $|v_{pL*}| \geq |v_{pL}|$ is more likely than $|v_{pL*}| < |v_{pL}|$. Nevertheless, by this linear analysis $|v_{pL*}| < |v_{pL}|$ cannot be ruled out.

Applying the linear analysis to estimate $|v_{pM*}|$ from Equation (14) and $|v_{pA*}|$ from Equation (15)) yields estimates of C_{M*} and C_{A*} ranging (conservatively) between 10^{-2} to 10^2. Interpreting such a wide range of possibilities is difficult. Nevertheless, this does suggest that the nonlinear models may be more sensitive to the temperature and moisture dynamics than the linear model. Further comparisons between all of these induced advective velocities is deferred until the discussion of the numerical results.

2.2.3 A semi-observationally-based approach to estimating v_p

This section outlines semi-observationally-based approach, based on vertically integrating the conservation of mass (the COM approach), for estimating the advective velocities. It provides an alternative method that complements the three models outlined above. It follows from an approach similar to that employed by Parlange et al. (1998) and Novak (2016) for assessing how the diel cycle of v_T and v_θ might influence rates of soil moisture evaporation.

By integrating the 1-D version of Equation (2) over depth (after disregarding **J** and S_a as discussed) the COM approach becomes

$$Q_a(z=0) - Q_a(z_r) = -\int_{z_r}^{z=0}\left(\frac{\partial\big((\eta-\theta)\varrho_a\big)}{\partial t}\right)dz \tag{17}$$

where $Q_a = (\eta-\theta)\varrho_a v$ (mol m^{-2}s^{-1}) is the advective soil air mass flux, z_r (m) is a reference depth in the soil and $z=0$ refers to the soil surface. Because this study uses $v(0)$ as a metric for assessing the relative performance of the three different models z_r is chosen to be the lower boundary of the model domain = 20 m at which the soil permeability (discussed in the next section) becomes small enough to assume that $|Q_a(z=0)| \gg |Q_a(z_r)|$ or $|v(z=0)| \gg |v(z_r)|$. With this lower boundary condition and the ideal gas law, Equation (17) can be solved for $v(0)$ to yield

$$v(0) = -\frac{1}{\big(\eta(0)-\theta(0)\big)\varrho_a(0)}\int_{z_r}^{z=0}\left((\eta-\theta)\frac{\varrho_a}{P_a}\frac{\partial p_\beta}{\partial t} - (\eta-\theta)\frac{\varrho_a}{T_K}\frac{\partial T_\beta}{\partial t} - \varrho_a\frac{\partial\theta_\beta}{\partial t}\right)dz \tag{18}$$

Equation (18) has the advantage of being linear in the forcing functions related to pressure, temperature and moisture. Therefore, it is also possible to identify $v_p(t,0)$, $v_T(t,0)$ and $v_\theta(t,0)$ as follows:

$$v_p(0) = -\frac{1}{\big(\eta(0)-\theta(0)\big)\varrho_a(0)}\int_{z_r}^{z=0}\left((\eta-\theta)\frac{\varrho_a}{P_a}\frac{\partial p_\beta}{\partial t}\right)dz \tag{19}$$

$$v_T(0) = \frac{1}{\big(\eta(0) - \theta(0)\big)\varrho_a(0)} \int_{z_r}^{z=0} \left((\eta - \theta) \frac{\varrho_a}{T_K} \frac{\partial T_\beta}{\partial t} \right) dz \tag{20}$$

and

$$v_\theta(0) = \frac{1}{\big(\eta(0) - \theta(0)\big)\varrho_a(0)} \int_{z_r}^{z=0} \left(\varrho_a \frac{\partial \theta_\beta}{\partial t} \right) dz \tag{21}$$

where the analytical models for $T_K = T_K(t,z)$, $T_\beta = T_\beta(t,z)$, $\theta = \theta(t,z)$ and $\theta_\beta = \theta_\beta(t,z)$ (detailed above) are used with Equations (18) - (21). Note for consistency with previous notation that $v_{T\theta}(0) = v_T(0) + v_\theta(0)$ and $v_{p*}(0) = v_p(0) + v_T(0) + v_\theta(0)$.

To estimate $v_p(0)$ requires an model of $p_\beta(t,z)$, which here is the product of the upper boundary condition on pressure $p_\beta(t,0)$ and an analytical expression for the attenuation of the surface pressure signal with depth. Thus $p_\beta(t,z) = p_\beta(t,0)\exp(-z/D_p)$, where now D_p depends on frequency range of the input signal. For low frequencies, $D_p \equiv D_{p,low} = 75$ m, for the mid range $D_p \equiv D_{p,mid} = 30$ m and for the high frequencies $D_p \equiv D_{p,high} = 1$ m. Although reasonable (as will be discussed further in section 4), these estimates of D_p are at this point "best guess only". Of the three only $D_{p,mid}$ could be estimated from the profile of observed soil pressures, i.e., the surface pressure plus pressure measurements at 0.1 m, 0.2 m and 0.5 m. Given the relatively shallow depths of the measurements compared to the magnitude of $D_{p,mid}$ and the fact that the sensor at 0.5 m was intermittent $D_{p,mid} = 30$ m is certainly plausible, but highly uncertain. Even less certain are the estimates of $D_{p,low}$ and $D_{p,high}$. $D_{p,low}$ is scaled from $D_{p,mid} = 30$ m by a frequency ratio of the low and mid frequencies and $D_{p,high} = 1$ m is obtained from near-surface soil permeability measurements at MEF (Appendix B) and by assuming that the dominant high frequency pressure forcing has a period of 1-3 minutes. Given the large uncertainties inherent in these estimates of D_p, each is compared with the numerical results. Finally, $\partial p_\beta(t,z)/\partial t$ is computed numerically using a third order finite difference scheme, $\partial p_\beta(t,z)/\partial z$ is computed analytically and the integration uses MatLab subroutines.

3 Site Description, Instrumentation, and Data

Manitou Experimental Forest (39° 04′ N and 105° 04′ W) is a dry montane ponderosa pine (*Pinus ponderosa*) forest in the central Rocky Mountains about 45 km west of Colorado Springs, CO, USA. MEF has a mean elevation of about 2400 m ASL, an annual mean temperature of about 5 C and an annual precipitation of about 400 mm. Previous grazing and mechanical harvesting throughout the area has resulted in a moderately disturbed soil. Soil organic matter comprises about 1-2% of the soil by mass and is more or less uniform through at least the top 10 cm of soil. The dominant parent materials of the soils within MEF are primarily Pikes Peak granite and secondarily weathered red arkostic sandstone. Typical soil within MEF is a deep (> 1.0 m), fine-loamy, mixed, frigid, Pachic Argiustoll and tend to have low available water holding capacity and a (moderately high) permeability – ranging between about $1{\times}10^{-12}$ and $250{\times}10^{-12}$ within the top 1 m of the soil. Typical MEF soils range between 60-65% sand, 20-25% silt, and 10-15% clay with bulk densities that usually increase with depth and range between 1.1 Mgm^{-3} and about 1.6 Mgm^{-3}. For modeling purposes the vertical structure for the soil permeability, $k_u(z)$, and bulk density, $\rho_s(z)$, are derived from measurements of their vertical profiles obtained in the upper 1 m of soil at MEF (see Appendix B). These analytical functions are $k_u(z) = 10^{-12}(126\tanh(6(z-0.95)) + 132.4)$ m^2 in the upper 1.5 m and as $k(z) = k_u(z=1.5)\exp(-(z-1.5))$ for 1.5 m $\le z \le$ 20 m and $\rho_s(z)$, as $1.65 + \sin(\pi(z+7/60))(\tanh(4(z-0.72)) - 1)/3$ Mgm^{-3} throughout the domain. The model for the total soil porosity, $\eta = \eta(z)$, follows directly from the $\rho_s(z)$, i.e., $\eta(z) =$

$1-\rho_s(z)/\rho_p$, where $\rho_p = 2.65$ Mgm^{-3} is the particle density for the sandy MEF soils, which is assumed to be constant throughout the domain.

The data supporting the present study is part of a larger (multi-purposed) field campaign performed between December 2008 and August 2014 (Frank & Massman, 2020). The specific site was on a gentle east facing slope about 1.2 km west of the Manitou Experimental Forest headquarters in an opening covered primarily by bunchgrasses, but with a few scattered trees throughout. All sensors were confined to a 15 m × 15 m plot. At the center of the plot was an elevated structure with control boxes, dataloggers, solar panels, and batteries. Replicate soil pits were located in four directions about 4 m from the center. Each replicate had three pits, the first was about 1.3 m deep for temperature (and thermal conductivity probes, which are not discussed in the present study), a second for soil moisture probes that was about 1 m deep, and a third one for soil CO_2 probes that was about 1 m deep (which are not discussed here either). A final pit was dug for soil pressure sensors about 9 m east of the plot center that was about 1 m deep and large enough to hold a 0.5 m × 0.5 m sensor/control box. Profiles of the within-pore air pressure were sampled and recorded at 1 Hz at 0, 10, 20, and 50 cm with a differential pressure sensor (Appendix C). Profiles of soil temperature and soil moisture were measured and recorded every 5 minutes. Temperatures were measured with thermocouples at the soil surface and at 0.5, 1.5, 2.5, 3.5 7.5, 12,5 17.5, 25.0, 75.0, and 125.0 cm depths at four locations. Soil moisture was measured with TDRs (Time Domain Reflectometers) at 2.0, 5.0, 10.0, 15.0, 20.0, 50.0, 100.0 cm also at the same four locations. The full profiles of temperature and the soil moisture are important to the present study because they were used to check that the models for $T_\beta(t,z)$, $\theta_\beta(t,z)$, $\Lambda_t(t,z)$ and $\Lambda_z(t,z)$ (discussed in section 2.1.2 above) were reasonably consistent with the observed profiles.

Further details of the instrumentation and the experiment can be found in (Frank & Massman, 2020) and Appendix C, which summarizes the details about the pressure sensors and how the 1 Hz differential pressure data were calibrated against and merged with the low frequency (ambient) data used in the following section.

4 Results and Discussion

This study focuses on two periods in 2012: June 14-20 (144 hours) and October 2-13 (250 hours). The observationally-based surface forcing functions, $p_\beta(t,0)$, $T_\beta(t,0)$ and $\theta_\beta(t,0)$ are shown in Figures 1 (June) and 2 (October). The conservation of mass approach, Equations (18)-(21), and each of the three numerical models, Equations (7), (10), and (11), were used to estimate the surface velocity, $v(t,0)$ and the standard deviation of the surface velocity, $\sigma_v(0)$, for each period with pressure-only forcing and with pressure plus temperature and moisture effects. (Note: Henceforth $|v|$ or $|v(0)|$ (from the Linear Analysis section and understood here as the amplitude of a time series) and the standard deviation, σ_v or $\sigma_v(0)$, are used synonymously because for sinusoidal time series the amplitude and standard deviation are linearly related by $\sqrt{2}$.) All resulting standard deviations can be found in Table 1 including those associated with using the unfiltered 1 Hz surface data (all frequencies) and the filtered (low, mid, and high frequencies) surface pressure data as the upper (surface) boundary condition. Table 1 also includes $\sigma_{v_T}(0)$, $\sigma_{v_\theta}(0)$ and $\sigma_{v_{T\theta}}(0)$ and the results of a sensitivity analysis of $\sigma_{v_p}(0)$ to changes to the numerical value of $D_{p,high}$. The numerical results concerning $v(t,0)$ are shown and discussed in the next two sections.

4.1 Low frequency forcing: Periods ≥ 5 hours

Figure 3 shows the COM estimates of $v_p(0)$ from Equation (19), $v_T(0)$ from Equation (20) and $v_\theta(0)$ from Equation (21) for the June 2012 study period. The takeaways here are that (1) $|v_p| >> |v_T|$ and $|v_\theta|$, as might be expected for a soil with a permeability $> 10^{-12}$ m^2, and (2) the COM estimate of $|v_T|$ agrees more closely with Kim-

ball (1983) than with the estimated based of the thermally induced flow (Section 2.2.1 above). A less obvious takeaway is that during periods of rain (also see Figure 1 and in particular Figure 2) that $|v_\theta| \approx |v_T|$. In fact the corresponding figure for the October study period (not shown) would even indicate that $|v_\theta| > |v_T|$, a conclusion supported by the results shown in Table 1 (Low Frequencies column). There are two contributing factors to the unexpected reversal of this inequality. (a) v_T is smaller in magnitude during the October period than the June period because the soil is heated less strongly by the daily heating cycle during October than June (compare amplitudes of the soil surface temperatures shown in Figures 1b and 2b). (b) Although it is possible that lack of a temperature correction to the TDR may be contributing biased estimates of $\partial\theta/\partial t$ and $\partial\theta/\partial z$, there are two more important reasons why $|v_\theta|$ is relatively large during the October study period. First, rainfall amounts and rates were higher than during the June period and (2) the air filled pore space – the denominator of Equation (21), $\eta(0)-\theta(0)$ – is smaller during the October period, which will tend to increase $|v_\theta|$.

These low frequency results from the COM approach are echoed in $\sigma_v(0)$ in Table 1. In addition, this table further suggest that $\sigma_{v_{T\theta}} < \sigma_{v_T} + \sigma_{v_\theta}$, thereby supporting the notion that there is some phase difference between v_T and v_θ and that during a typical diel cycle the temperature and moisture effects tend to act (at least weakly) in opposition to one another. But Table 1 also indicates that v_θ can be surprisingly large (relative to v_T), undoubtedly due (at least in part) to rapid changes in soil moisture associated with rain. Finally, the influence of soil heating and moisture dynamics on $|v_p|$ (see Equation (18)) is also presented in Table 1 (by comparing σ_{v_p} with $\sigma_{v_{p*}}$ in the All and Low Frequencies columns). Overall temperature and moisture effects do not have much impact on the pressure pumping velocity for the COM approach. But during periods of rapid changes in θ soil moisture dynamics may be important enough to consider, especially if the soil is moist to begin with or if the soil permeability is $< 10^{-12}$ m^2.

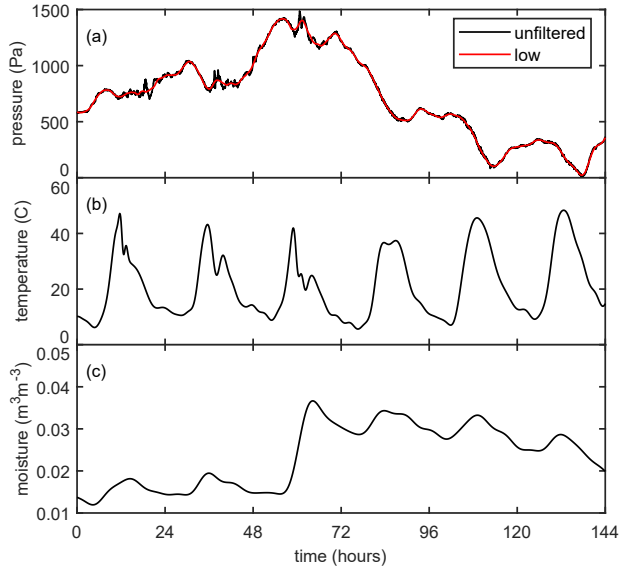

Figure 1. Model drivers (or surface forcing functions) for the June 14-20, 2012 simulation. (a) The black line is the observed 1 Hz surface pressure data, $p_\beta(t,0)$, which has had enough of the background pressure removed to ensure all data are ≥ 0. The red line is the numerically filtered low frequency component of the surface pressure and includes only those data with periods ≥ 5 hours. (b) 1 Hz temperature forcing function, $T_\beta(t,0)$, interpolated from the observed 5 minute averages of the soil surface temperatures. The frequency content of this forcing is limited almost exclusively to low frequencies with only a small component of mid frequency content (i.e., periods between 0.5 and 5 hours). (c) 1 Hz soil moisture forcing function, $\theta_\beta(t,0)$, interpolated from the observed 5 minute averages of the 2-cm volumetric soil moisture. This forcing is exclusively low frequency because the mid and high frequency content (i.e,. with periods between 1 s and 0.5 hours) was low amplitude noise that has no influence on the numerical results.

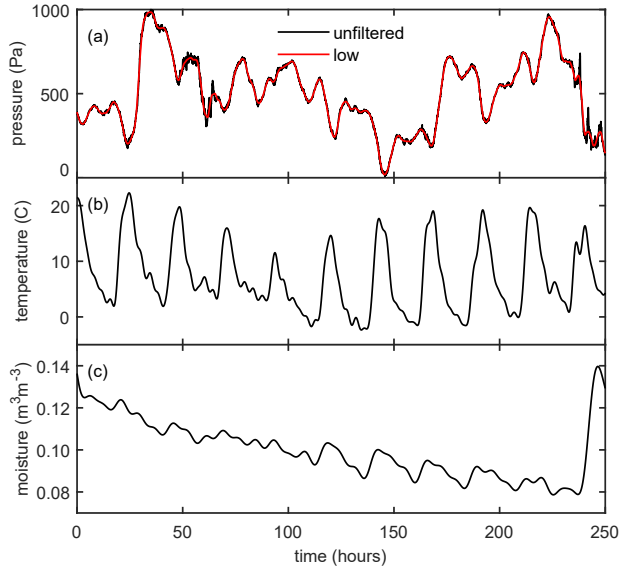

Figure 2. Model drivers (or surface forcing functions) for the October 2-13, 2012 simulation. (a) The black line is the observed 1 Hz surface pressure data, $p_\beta(t,0)$, which has had enough of the background pressure removed to ensure all data ≥ 0. The red line is the numerically filtered low frequency component of the surface pressure and includes only those data with periods ≥ 5 hours. (b) 1 Hz temperature forcing function, $T_\beta(t,0)$, interpolated from the observed 5 minute averages of the soil surface temperatures. The frequency content of this forcing is limited almost exclusively to low frequencies with only a small component of mid frequency content (i.e., periods between 0.5 and 5 hours). (c) 1 Hz soil moisture forcing function, $\theta_\beta(t,0)$, interpolated from the observed 5 minute averages of the 2-cm volumetric soil moisture. This forcing is exclusively low frequencies because the mid and high frequency content (i.e,. with periods between 1 s and 0.5 hours) was low amplitude noise that has no influence on the numerical results.

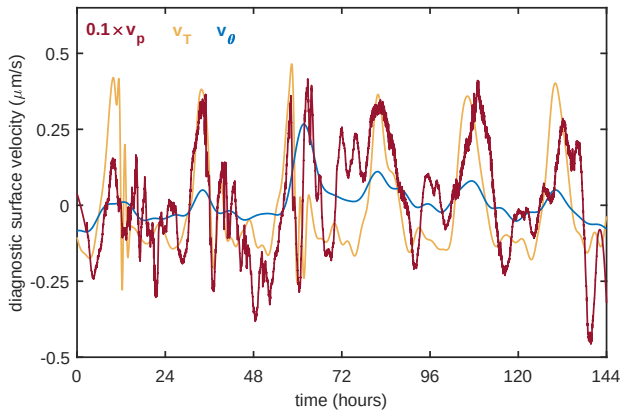

Figure 3. Estimates of low frequency advective velocities induced by pressure, temperature and soil moisture dynamics using the COM approach (Equations (19), (20), and (21)) for June 14-20, 2012. As discussed in the text, the soil temperature and moisture forcing functions, and therefore, v_T and v_θ as well, are for all numerical purposes low frequency only.

Table 1. Standard deviation of soil surface advective velocity variance: $\sigma_v(0)$ (μms^{-1}). The subscript $*$ denotes the inclusion of the temperature and moisture effects. [a] $\sigma_{v_{T\theta}} = \sigma\big(v_T + v_\theta\big)$; [b] $\sigma_{v_p} = \sigma\big(v_{p,low} + v_{p,mid} + v_{p,high}\big)$; [c] $\sigma_{v_{p*}} = \sigma\big(v_{p,low} + v_{p,mid} + v_{p,high} + v_T + v_\theta\big)$. Note that numerical estimates for $\sigma_{v_T}(0)$, $\sigma_{v_\theta}(0)$ and $\sigma_{v_{T\theta}}(0)$ are the same for All Frequencies and Low Frequencies. This is because the frequency content of soil temperature and moisture is overwhelmingly low frequencies. The column relating to $D_{p,high}$ is part of a sesnitivity analysis regarding the COM's estimates of v_p.

Model	All Frequencies		Low Frequencies		Mid+High Frequencies		Mid Frequencies		High Frequencies		
	06/2012	10/2012	06/2012	10/2012	06/2012	10/2012	06/2012	10/2012	06/2012	10/2012	$D_{p,high}$ (m)
COM											
σ_{v_T}	0.17	0.07	0.17	0.07	—	—	—	—	—	—	
σ_{v_θ}	0.06	0.11	0.06	0.11	—	—	—	—	—	—	
$\sigma_{v_{T\theta}}$	0.20[a]	0.14[a]	0.20[a]	0.14[a]	—	—	—	—	—	—	
σ_{v_p}	5.6[b]	5.5[b]	1.7	2.7	—	—	2.3	2.7	4.8	4.0	1.0
$\sigma_{v_{p*}}$	5.7[c]	5.6[c]	1.9	2.7	—	—	—	—	—	—	—
σ_{v_p}	—	—	—	—	—	—	—	—	2.7	2.1	0.5
σ_{v_p}	—	—	—	—	—	—	—	—	3.6	4.4	0.9
σ_{v_p}	—	—	—	—	—	—	—	—	9.1	7.7	2.0
Linear											
$\sigma_{v_{pL}}$	4.4	4.1	1.5	1.8	4.2	3.6	1.8	1.7	3.7	3.2	
$\sigma_{v_{pL*}}$	3.0	2.6	0.9	1.0	—	—	—	—	—	—	
Muskat											
$\sigma_{v_{pM}}$	21	18	19	15	10	8.8	5.2	5.2	8.5	7.1	
$\sigma_{v_{pM*}}$	12	210	11	210	—	—	—	—	—	—	
Approximate											
$\sigma_{v_{pA}}$	19	15	17	13	9.7	8.4	4.7	4.6	8.5	7.0	
$\sigma_{v_{pA*}}$	11	175	10	175	—	—	—	—	—	—	

manuscript submitted to *JAMES*

Figure 4 compares (for June 2012) $v_p(t,0)$ from the COM approach (i.e, the COM approach and Equation (19)) with solutions from the Linear model, $v_{pL}(t,0)$ from Equation (7), the Muskat model, $v_{pM}(t,0)$ from Equation (10), and the Approximate model, $v_{pM}(t,0)$ from Equation (11). Figure 5 is the analog to Figure 4, except for the inclusion of the soil temperature and moisture dynamics in the solution, i.e., $v_{pL*}(t,0)$ from Equation (13), $v_{pM*}(t,0)$ from Equation (14) and $v_{pM*}(t,0)$ from Equation (15)). Comparing the first 80 hours of the these two simulations indicates that the temperature and moisture effects can alter the phase of the velocity or even reverse it completely and Table 1, which summarizes all low frequency modeling results for both the June and October 2012 observation periods, indicates that they can also affect the amplitude. With respect to the modeling results the important observations to make are (1) including heat and moisture effects with the two nonlinear models yield very different solutions for the October 2012 case than the June 2012 case. Otherwise, (2) for the June 2012 case the advective velocity associated with both the linear and nonlinear models decreases with the inclusion of temperature and moisture effects (i.e., $\sigma_{v_pL*} < \sigma_{v_pL}$, $\sigma_{v_pM*} < \sigma_{v_pM}$, $\sigma_{v_pA*} < \sigma_{v_pA}$), whereas the COM approach (very weakly) suggests just the opposite, (3) the Linear model and the COM approach produce velocities of a similar magnitude and phase but both are smaller in magnitude by a factor of 2 to 5 than either the Muskat or Approximate models and (4) the advective velocities associated with the Muskat model exceed those of the Approximate model. Some of these observations are valid for the October 2012 case as well, but the real difference is that for the October case σ_{v_pM*} and σ_{v_pA*} not only exceed σ_{v_pM} and σ_{v_pA}, but they both exceed 100 μms^{-1}, (possibly) contrary to expectations.

Accepting these unexpected results at face value suggests that temperature and moisture dynamics cannot always be ignored in the nonlinear models. But, to better understand this anomalous result a sensitivity analysis was performed that indicated that the nonlinear models' (Equations (14) and (15)) solutions were quite sensitive to the magnitude and vertical structure of Λ_z, but much less sensitive to variations in Λ_t. Regardless though none of these tests fully eliminated this seeming contradiction. However further insight into this quandary can be found in section 4.3, which deals with the models' profiles of pressure and advective velocity. Presumably additional insights might also be possible with a model that fully couples soil heating and moisture dynamics (rather than prescribing them as done here), but this avenue is beyond the purposes of the present study.

In addition to Table 1, the present (all and low frequency) results can be summarized by replacing Equation (16) with the following, more precise ordering of model advective velocities:

$$|v_\theta| \approx |v_T| \leq |v_{T\theta}| \ll |v_{pL*}| \leq |v_{pL}| \leq |v_p| \approx |v_{p*}| < \text{or} \ll |v_{pA}| \approx \text{or} < |v_{pM}| \qquad (22)$$

and

$$|v_{pA*}| < |v_{pM*}|$$

where $\ll$ signifies at least one order of magnitude difference and the relationships between $|v_{pA}|$ and $|v_{pA*}|$ and $|v_{pM}|$ and $|v_{pM*}|$ remain difficult to generalize with any certainty. But maybe this should not be unexpected. Recall that the linear analysis of section 2.2.2 was also unable to offer any easily generalized insights into what might be expected from any of the three models regarding the impact of including the heat and moisture effects on the relative magnitudes of their advective velocities.

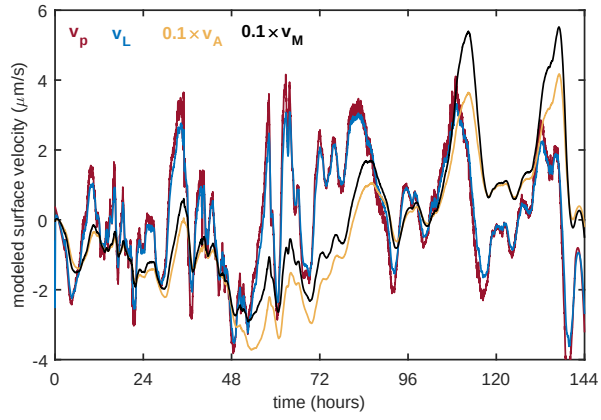

Figure 4. Estimates of low frequency advective velocities induced by pressure dynamics only using the Linear model (v_L, Equation (7)), the Muskat model (v_M, Equation (10)) and the Approximate model (v_A, Equation (11)) for June 14-20, 2012. v_p from the COM , Equation (19) is included for comparison.

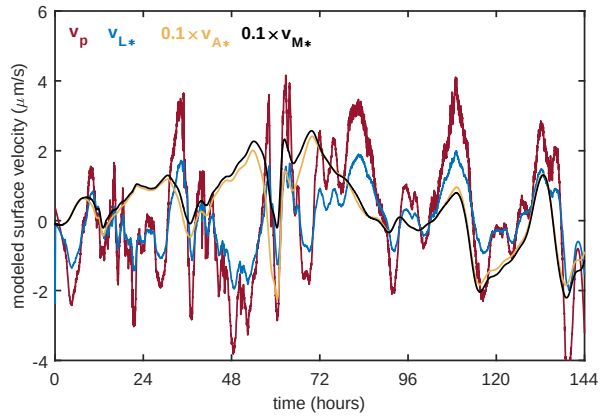

Figure 5. Estimates of low frequency advective velocities induced by pressure, temperature and soil moisture dynamics combined using the Linear model (v_{L*}, Equation (13)), the Muskat model (v_{M*}, Equation (14)) and the Approximate model (v_{L*}, Equation (15)) for June 14-20, 2012. v_p from the COM, Equation (19) is included for comparison.

But the implications of Table 1 extend beyond Equation (22). Recalling the discussion of the threshold velocity of 100 μms^{-1} (Section 2) and focusing on the COM approach and the linear model, it is possible to conclude that soil temperature and moisture dynamics are unlikely to ever play a role in advective flow in soils. Considering that Parlange et al. (1998) used the COM approach to conclude that temperature dynamics are a potentially significant contributor to advective flows in soils, the present results concur with Novak (2016), who pointed out that Parlange et al. (1998) must have made a computational error. Nonetheless, without further insights into causes of the unexpected results from the nonlinear models for the October 2012 case, the possibility remains that soil heating and moisture dynamics (Λ_z in particular) may enhance the advective velocities associated with pressure pumping enough (at least for the nonlinear models) that they might contribute to soil evaporation and the surface energy balance (i.e., $v_{pM*} > 100\,\mu$ms^{-1} and $v_{pA*} > 100\,\mu$ms^{-1}).

4.2 Mid (0.5 - 5 hrs) and high (1 s - 0.5 hrs) frequency forcing

Figure 6a shows a wavelet decomposition of the June 14-20, 2012 surface pressure after removal of the low frequency component. Figures 6b and 6c are (in order) the bandpass filtered mid and high frequency pressure components. This 6 day period can be partitioned into before (0–72 hours) and after (72–144 hours) a frontal passage (see the UCAR weather archives at https://www2.mmm.ucar.edu/imagearchive/) with rain falling for a short time beginning at about hour 60 (MEF headquarters building rain gauge). The three pressure events preceding the frontal passage are self-identified here as inertia-gravity waves (or possibly other related types of mesoscale gravity waves), whereas after the frontal passage the pressure perturbations are interpreted as a "typical" diel cycle of turbulence and other high frequency atmospheric phenomena. The presence of inertial gravity waves during this period of frontal activity and associated convective activity is almost a certainty (e.g., Koch and Siedlarz (1999); Ralph et al. (1999); Koppel et al. (2000); Ruppert and Bosart (2014); X. Wang et al. (2020)). Further fitting a Morlet function (modulated wave packet) to each of these inertia gravity wave events yields wave periods between about 2.1 and 2.5 hours with amplitudes between approximately 30 and 70 Pa, which are very similar to the low frequency gravity waves observed in China by X. Wang et al. (2020) and very similar to an inertia-gravity wave's theoretical period of about 2.7 hours (at 45° N latitude) suggested by Fritts and Alexander (2003).

Given the near ubiquity of inertia-gravity waves and their close association with convective frontal systems, Figure 7 examines how this phenomenon might influence advective flows (at least in the MEF soils) by isolating the first 48 hours of the June 2012 study period. This figure includes the mid frequency surface forcing and the modeled mid and high frequency response (surface velocities). The important takeaways from Figures 6 and 7 are (1) the mid and high frequency velocities computed with the nonlinear models exceed by an order of magnitude the velocities produced by the linear model and the COM approach (also see Table 1), (2) both the mid and high frequency instantaneous velocities are significant, often approaching or exceeding the critical 100 μms^{-1} velocity, especially with the nonlinear models for which the velocities can approach 1000 μms^{-1}, (3) the mid frequency forcing events seem to intensify (or be associated with) some of the high frequency pressure forcing (including the diel cycle of turbulence), and (4) what might otherwise appear in a shorter time series as more-or-less random episodic pressure forcing events appear in these figures to result from causal atmospheric phenomena, which are often associated with frontal systems, thunderstorms and rain.

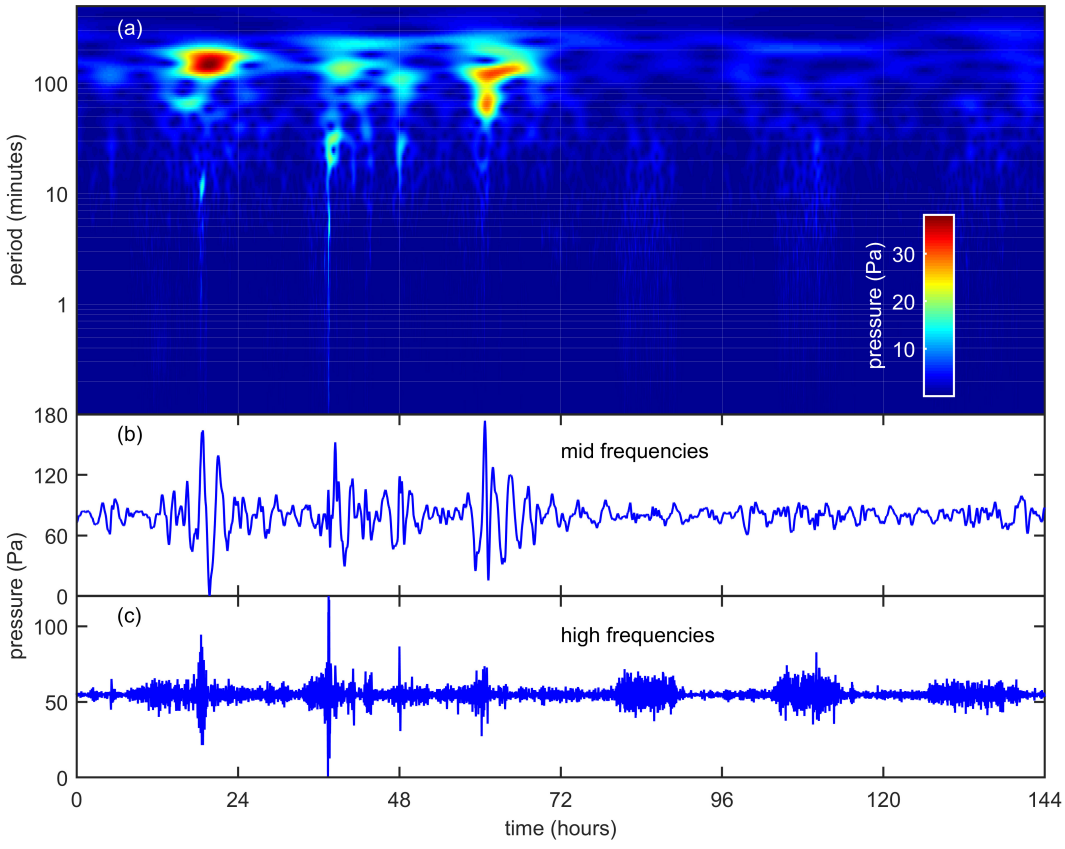

Figure 6. (a) Wavelet decomposition of the June 14-19, 2012, soil surface pressure time trace using the Morlet wavelet after removing the low frequencies, i.e., all frequencies with periods longer than 5 hours. (b) Filtered mid frequency (periods between 0.5 and 5 hours) surface pressure time series. (c) Filtered high frequency (periods between 1 s and 0.5 hours) surface pressure time series. Three (self-identified) inertia-gravity waves occur each day during the first 72 hours (June 14, 15, 16). Wave periods of these events (panels (b)) were between about 2.1 and 2.5 hours with maximum amplitudes between approximately 30 and 70 Pa. Rain fell about hour 60 (mid-day June 16). The daily pulses of high frequency surface pressure, panel (c), during the last 72 hours (June 17, 18, 19) are interpreted here as the diel cycle in turbulence, suggesting that the three wave events (panel (b)) intensify the diel cycle of turbulence. Finally, in addition to the inertia-gravity wave the second day (panel (b)) appears to include a slightly higher frequency gravity wave event centered at about 48 hours.

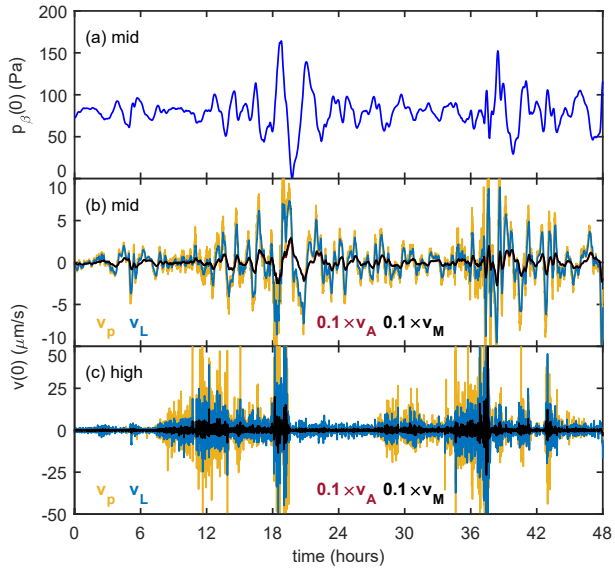

Figure 7. (a) First 48 hours of the June 2012 mid-frequency soil surface pressure time series. The surface pressure perturbations between approximately 16 and 24 hours and the more complex signal between about 36 and 48 hours are interpreted here as an inertia-gravity wave events. These two wave events coincide with the leftmost (first and second) 'bright spots' on Figure 6a. (b) First 48 hours of the modeled June 2012 mid frequency soil surface velocities and (c) first 48 hours of the modeled high frequency surface velocities. Because $v_A \leq v_M$, v_A is obscured by v_M in panel (c). All velocities highlight the impact that the inertia-gravity waves, shown in panel (a), can have on the soil advective velocity field. Note the episodic nature of the high frequency velocities, their (at least partial) association with the wave events, and that the high frequency velocities are often about an order of magnitude greater than the mid-frequency velocities.

Figures 8 and 9 are the October analog to the two preceding figures. Figure 8 suggests that an inertia gravity wave event occurred during each of the first two days of the October period (i.e., October 2 and 3). This wave activity occurred ahead of the passage of a weak wind shift line and frontal system (UCAR weather archives: https://www2.mmm.ucar.edu/imagearchive/). The wave periods of these two events were between about 2.2 and 2.6 hours with amplitudes between approximately 20 and 60 Pa, quite similar to the June events. But Figure 8 also suggests something quite different appeared on the last day of the study period, October 13. The two obvious pressure spikes on that day (and possibly two or three less obvious spikes, which precede and follow the two major spikes) are here self-identified as atmospheric solitons. Solitons or solitary waves, are identified as either positive or negative pressure pulses (or spikes) and often associated with fronts and thunderstorms (e.g., Shreffler and Binkowski (1981); Doviak and Ge (1984)). They can have amplitudes between about 10 and 200 Pa with a duration between about 10 minutes and 2 hours (e.g., Goncharov and Matveyev (1982); Hauf et al. (1996); Ruppert and Bosart (2014)). Figure 9 isolates these solitons (panel a) and the mid and high frequency modeled soil advective velocities in the last 25 hours of the October 2012 study period. The amplitudes of these two events are between about 80 and 110 Pa with durations between about 1.6 and 2 hours. On this day there was significant frontal activity in the area (https://www2.mmm.ucar.edu/imagearchive/) with rain starting just in the early afternoon (MEF rain gauge). The takeaways from this October period (i.e., last two figures) are the same as the June period, except that the intensification of the high frequency forcing and associated soil velocities by the mid frequency events is even stronger.

Figure 10 and Table 1 summarize the June and October modeling results for the three frequency ranges. Figure 10 especially highlights the difference between the nonlinear and linear methods. First $\sigma_v(0)$ from the nonlinear models always exceed those predicted by linear methods and second, the ratio $\sigma_{vL}(0)/\sigma_{vM}(0)$ is much smaller at low frequencies than at mid or high frequencies. The first of these relationships was anticipated by the linear analysis discussed in section 2.2.2, but the second is opposite of what was predicted. Possibly this should not be too surprising because the linear analysis cannot fully describe the solutions of the nonlinear models. The interpretation of the results given in Figure 10 is that the nonlinear models produce significantly greater advective transport at low and high frequencies than at mid frequencies. In fact, the difference between modeling results at low frequencies is so great that it is possible to conclude that pressure induced advective motions in soils is likely negligible for the linear model (contrary to expectations), whereas just the opposite conclusion can be reached with the nonlinear models. A complementary interpretation to this is that the linear methods produce greater advective transport at the mid/high frequencies than at low frequencies. Overall, these rather different "spectral responses" again serve to emphasize that the linear and nonlinear models are fundamentally different models of pressure pumping and, as a consequence, they yield different predictions for the advective velocities in permeable media.

The point was made earlier that all the estimates for D_p used with the COM approach were fairly uncertain. Consequently the estimates of the advective velocities associated with the COM approach are also uncertain. This is especially true for high frequencies because the range of variation in D_p is greatest for high frequencies. To address this Table 1 includes estimates of the high frequency (COM) σ_{vp} for $D_p = 0.5$ m and $D_p = 2.0$ m. (Recall that $D_p = 1.0$ m is the original estimate (Table 1)). This sensitivity analysis (change in σ_{vp} with respect to change in D_p) for high frequencies qualifies the results shown in Figure 10. At least for high frequencies, even small change in a reasonable guess for D_p could yield an estimate of σ_{vp} that more closely resembles (or even exceeds) σ_{vpM} and σ_{vpA} (the nonlinear models) than σ_{vpL} (the Linear model). Consequently, imprecise knowledge of D_p only yields imprecise estimates of the advective velocity associated with the COM approach and any ability it may have to distinguish

between linear and nonlinear models is potentially lost, especially at high frequencies. But the relationship between the COM, D_p, and $v_p(z)$ at high frequencies is more confusing than might otherwise be expected from just this section.

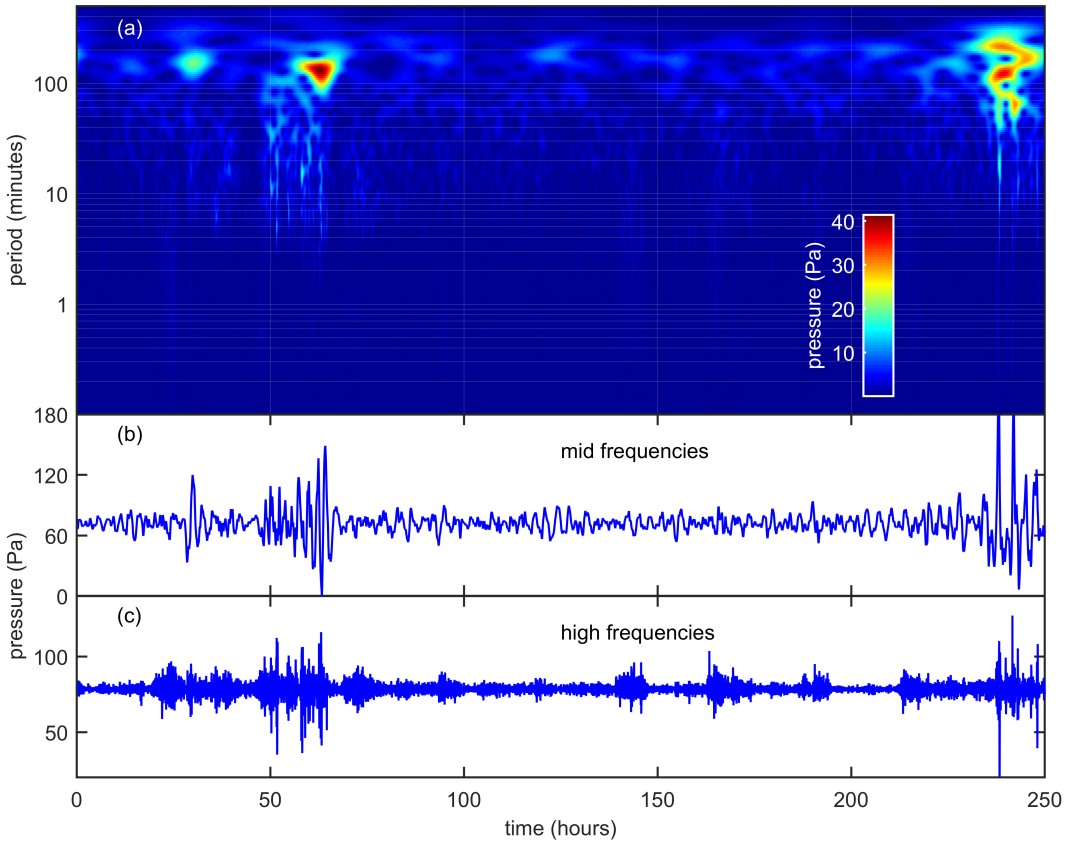

Figure 8. (a) Wavelet decomposition of the October 2-13, 2012, soil surface pressure time trace using the Morlet wavelet after removing the low frequencies, i.e., all frequencies with periods longer than 5 hours. (b) Filtered mid frequency (periods between 0.5 and 5 hours) surface pressure time series. (c) Filtered high frequency (periods between 1 s and 0.5 hours) surface pressure time series. Two (self-identified) inertia-gravity waves occur each day between (approximately) 24 and 72 hours (October 3 and 4). Wave periods of these two waves, panel (b), were between about 2.2 and 2.6 hours with maximum amplitudes between approximately 20 and 60 Pa. A pair of atmospheric solitons (also self-identified) appear as two positive spikes in panel (b), the mid-frequency time series, during the last 24 hours (October 13). The amplitudes of these two events are between about 80 and 110 Pa with durations between about 1.6 and 2 hours. Rain fell just after hour 240 (mid-day October 13). Similar to the June study period (Figure 6c), the diel cycle of turbulence is also present during the October period and again both the inertia-gravity waves and the solitons appear to intensify the high frequency turbulent surface pressure perturbations.

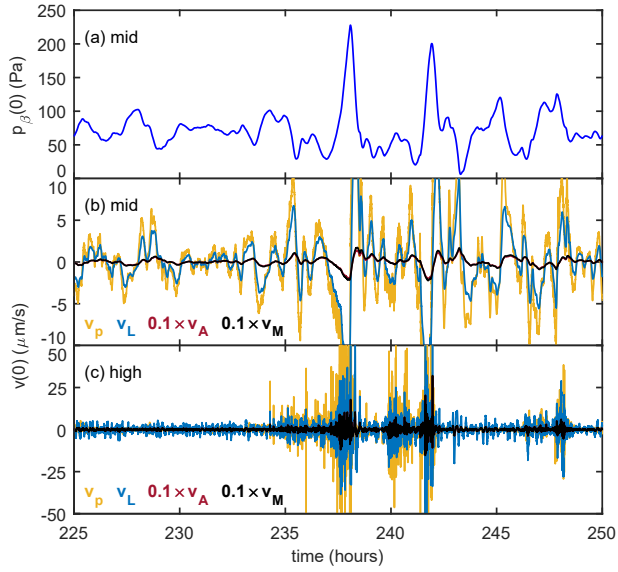

Figure 9. (a) Last 25 hours of the October 2012 soil surface pressure time series. The two pressure events centered at approximately 237 and 243 hours are interpreted here as solitons and they correspond to the rightmost (complex) 'bright spot' on Figure 8(a). (b) Last 25 hours of the modeled (b) mid frequency soil surface velocities and (c) high frequency soil surface velocity time series. Because $v_A \leq v_M$ v_A is obscured by v_M in panel (c). All velocities highlight the impact that the solitons, shown in panel (a), can have on the soil advective velocity field. Note the episodic nature of the high frequency velocities, their (relatively) strong association with the soliton events, and that the high frequency velocities are often about a factor of two or more greater in magnitude than the mid-frequency velocities.

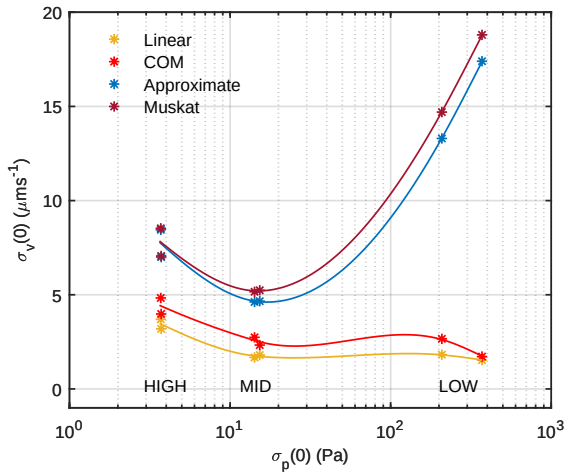

Figure 10. Summary plot of the response, $\sigma_v(0)$, vs the forcing, $\ln(\sigma_p(0))$, for the June and October study periods as a function of frequency band for the COM approach, the linear model and the two nonlinear models. Low frequencies refer to atmospheric pressure variations with periods $\geq$ 5 hours, mid frequencies have periods between 0.5 and 5 hours, and high frequencies have periods between 1 sec and 0.5 hours. Given that $\sigma_p(0)$ increases fairly strongly with decreasing frequency this plot can also be interpreted as a crude description of the different models' spectral response.

4.3 Vertical profiles of pressure and advective velocity

For the same surface forcing and permeability the reason the nonlinear models predict a higher amplitude for the advective velocities than the linear methods can be inferred from Figure 11, which shows the modeled vertical profiles of the normalized standard deviation of pressure for the top 8 m of the model domain during the June 14-20, 2012 study period. Although difficult to tell from the high frequencies (Figure 11c), this figure indicates that, regardless of the forcing frequency, within the top 1 m or so the surface pressure attenuates with depth more strongly with the nonlinear models than do either the Linear model or COM approach. This difference in near-surface pressure gradients is made more obvious in Figure 12, which shows the modeled vertical profiles of $\sigma_v(z)$ for the top 8 m of the model domain during the June 14-20, 2012 study period. All profiles in this figure show a maximum at approximately 1.4 m, which corresponds to the maximum in the MEF soil permeability of approximately two orders of magnitude greater than the very-near surface permeability (Appendix B).

Figure 11c also offers an insight into the COM approach. Although not shown here, within the top meter of the domain the nonlinear $D_{p,high} \approx 0.9$ m, whereas the linear $D_{p,high} \approx 2$ m. But as shown in Table 1, σ_{vp} for $D_{p,high} = 2$ m (linear model) agrees more closely with the nonlinear estimate of σ_{vp} than it does with the linear estimate and vice versa for $D_{p,high} = 0.9$ m (nonlinear model). In other words, the ability of the COM to distinguish between the linear and nonlinear models, or to offer any insights for preferring one type of model over the other, is not only lost at high frequencies, it yields inferences that are completely opposite of model-based expectations. This same reversal occurs with the COM with the mid- and low frequencies, but σ_{vp} is much less sensitive to variations (or uncertainties) in $D_{p,mid}$ or $D_{p,low}$, so the COM resembles the linear model more than the nonlinear models.

For those cases that do not include soil heat and moisture dynamics these last Figures 10 and 11 are elaborations of the results summarized in Table 1 and Equation (22). But the differences between the linear and nonlinear approaches is more complicated when heat and moisture effects are included, e.g., Figure 13, which shows that heat and moisture dynamics have very little impact on the Linear model, but for the two nonlinear models its impact on the vertical structure of the pressure gradient and the advective velocity are more significant. Both the surface gradient, or equivalently the surface velocities – Table 1, rows v_{pM*} and v_{pA*}, June and October study periods – and the general overall gradient (compare Figures 11, 12 and 13) suggest that the nonlinear models are fairly sensitive to heat and moisture dynamics. This may not be too surprising given that these are nonlinear hyperbolic models, e.g., Hinch (2020) and that $|\partial p_\beta/\partial z| \ll |\Lambda_z|$ (Equations (14) and (15)), which changes the nature of the non-linearity of these hyperbolic models. Present results suggests that heat and moisture dynamics have the potential to impact the nonlinear models' solutions, particularly in the upper meter or so of the soil profile. But the degree of sensitivity is more than (at least) these authors were expecting. It is difficult to generalize beyond this undistinguished conclusion concerning the nonlinear models' sensitivity. In part, this is because for the June study period v_{pM*} and v_{pA*} (Table 1) are more-or-less unsurprising and in agreement with expectations, whereas for the October study period they are one to two orders of magnitude greater than might have been expected. One possible explanation might be that the nonlinear models are unstable and, therefore, their solutions are physically unrealistic. The "jaggedness" (discontinuities) of the nonlinear models' vertical profiles shown in Figure 13 might support this notion. Furthermore, the authors' experience suggests that once model velocities begin to approach or exceed about 10 mms^{-1} (or 10^4 μms^{-1}) these models can become unstable. But decreasing the vertical spacing (from the current 0.10 m) did not produce any clear insights into these potential model instabilities or eliminate the discontinuities. Beyond this somewhat obvious conclusion that the nonlinear models' are relatively sen-

sitive to heat and moisture effects, present results offer only that more numerical and observational investigations seem warranted.

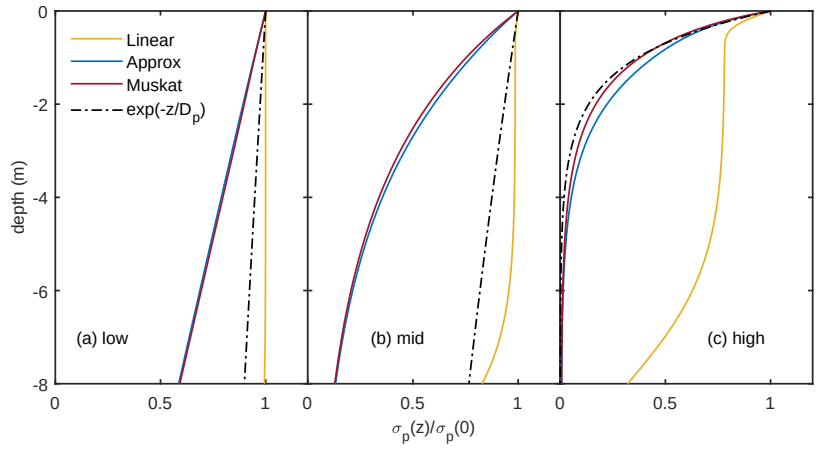

Figure 11. Modeled vertical profiles of the normalized standard deviation of pressure for the top 8 m of the model domain during the June 14-20, 2012 study period. The COM approach is identified by the expression $\exp(-z/D_p)$, where $D_p = 75$ m for the low frequencies, for mid frequencies $D_p = 30$ m, and D_p for the high frequencies is 1 m.

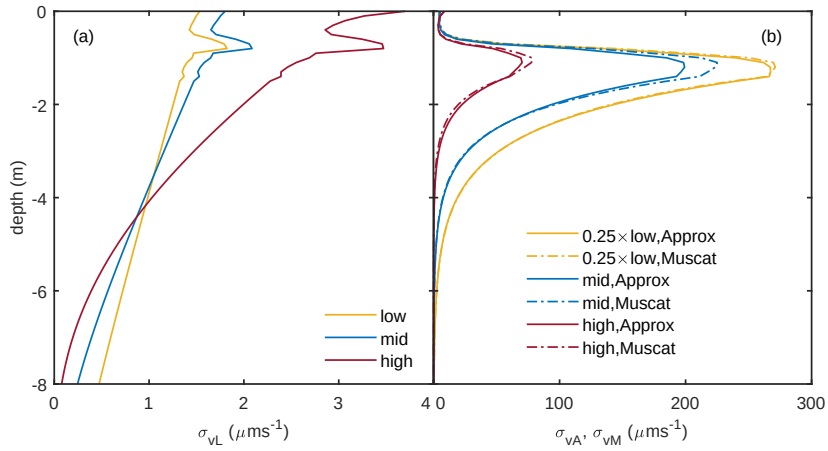

Figure 12. Modeled vertical profiles of the standard deviation of advective velocities for the top 8 m of the model domain during the June 14-20, 2012 study period. Panel (a) shows the low frequencies, (b) the mid frequencies and (c) for the high frequencies. All profiles show a maximum at approximately 1.4 m, which corresponds to the maximum in the MEF soil permeability of $k(-1.4) \approx 250 \times 10^{-12}$ m$^2 \approx 40 \times k(0)$. The second letter of each subscript refers to the model: 'L' is the linear model, 'A' is the approximate model (solid lines) and 'M' refers to the Muskat model (dash-dot lines).

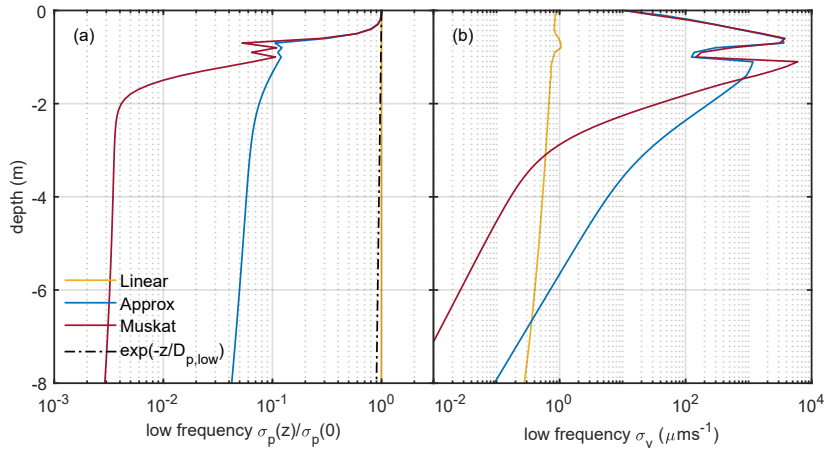

Figure 13. Low frequency (June 2012) modeled profiles in the top 8 m of the model domain with heat and moisture dynamics included (i.e., Equations (13), (14) and (15)). The COM approach is identified by the expression $\exp(-z/D_p)$, where $D_p = 75$ m for the low frequencies. Panel (a) shows the modeled vertical profiles of the normalized standard deviation of pressure and panel (b) the standard deviation of advective velocities.

5 Summary and Conclusions

(1) Model Comparisons: This study begins with a review of the physical fundamentals of two different categories of models used to describe pressure-induced advective (i.e., non-diffusive) gas flow in permeable media at the earth's surface. Both types of models have been used for decades to describe pressure pumping, but mathematically they are very different, with one model characterized as linear parabolic (Buckingham, 1904) and the other two, slightly different, models as nonlinear hyperbolic (Muskat, 1937; Kidder, 1957; J. W. Massmann, 1989). The linear model results from assuming that the flow field is compressible (i.e., $\nabla \bullet v \neq 0$) and the nonlinear models both assume that the flow field is incompressible (i.e., $\nabla \bullet v = 0$). The numerical results, summarized by Table 1 and Figure 10, were (mostly) anticipated by a linear analysis of the model equations (Section 2.2.2 and Equation (16)) and show that the nonlinear models will always yield advective velocities that are similar to one another but always greater than those of the linear model by approximately an order of magnitude and that the difference between these two types of models is greatest for low frequencies forcings (i.e., phenomena with periods $\geq$ 5 hours). In fact the differences were great enough to suggest that low frequency advective motions induced by pressure changes (for soils with permeability similar to those at MEF) is small enough in the Linear model to be neglected, contrary to expectations. On the other hand, low frequency advective motion within snowpacks is likely to be significant because the permeability of snowpacks is often two or more orders of magnitude greater than it is for MEF soils, i.e., $k_{snowpack} = (1 - 100)10^{-10}$ m^2 (e.g., Sommerfeld and Rocchio (1993); Albert and Shultz (2002)). For mid (periods between 0.5 and 5 hours) and high (periods between 1 s and 5 hours) frequencies the model differences are less, but are still significant. The vertical profiles of pressure and velocities were also very different with the nonlinear models associated with velocities of much greater magnitude, but more strongly attenuated, within the top 5 m of the soil than the Linear model. Overall, model-based numerical estimates of pressure induced trace gas exchange between the atmosphere and soils and snowpacks is strongly model dependent and, therefore, any quantitative results are potentially biased or incorrect.

Because the conservation of mass (COM) approach, Equation (19), is independent of the compressible/incompressible flow assumption it was originally hoped that it would provide some ability to discriminate (or choose) between the linear and nonlinear models. But this was not really the case, despite its apparent congruence with the Linear model, Equation (7). There are two principal reasons for this. First for high frequencies, using the best estimate of the Linear model's attenuation depth, D_p (the key input parameter of the COM), yielded an estimate of v_p that agreed more closely with nonlinear models and vice versa for the nonlinear models' best estimate of D_p. Second, although for low frequency surface forcing the COM agreed very closely with the Linear model, these velocities were so low compared to all other velocities as to suggest that the low frequency forcing is negligible, as mentioned in the previous paragraph.

(2) Heat and Moisture Dynamics: Changes in temperature and moisture can influence the pressure within the soil pore spaces (Equations (13), (14) and (15)) especially during the daily cycle (i.e., low frequencies). The Linear model showed very little sensitivity to these dynamics. Nonetheless, there was some suggestion that the advective velocity associated with soil moisture was surprisingly higher than what was expected, especially during rain events. The nonlinear models were far more sensitive to heat and moisture dynamics than the Linear model. In fact, these additional forcings enhanced the (already significant) nonlinear low frequency pressure-only advective velocities by an order of magnitude, which again was unanticipated. If this result could be observationally verified, it would suggest that interplay of the daily cycles of atmospheric forcing and soil heating is a significant driver of soil evaporation (from relatively moist soils, of course).

(3) Mid and High Frequency Forcing by Mesoscale Atmospheric Events: Both the linear and nonlinear models are unambiguous about the importance of mid and high frequency forcing to soil gas transport, with the linear model even suggesting that the transport at these frequencies are the dominant forcing frequencies. A novel contribution of the present study is the recognition that significant gas transport in soils is associated with and enhanced by mid-frequency mesoscale atmospheric phenomena, such as inertia-gravity waves and solitons (Figures 7 and 9). These phenomena, often generated by larger scale atmospheric events like thunderstorms and frontal systems, are important in their own right as forcings for transport. But they also intensify the diurnal cycle of turbulence, itself the key, high frequency, driver of soil gas transport. Thus further research into pressure pumping in soils and snowpacks should be aware of the significance of the mid-frequency forcings and their strong coupling to the high frequency forcing.

(4) A Summation: In the simplest terms and all other things being equal, the nonlinear models portray the action of the atmosphere on soil gas transport as significantly more dynamic and consequential than the linear models. Given the increasing need for understanding of climate change's influence on the intensification of hydrologic events, such as droughts and rainfall, on soil evaporation and respiration, it seems worthwhile to be aware of (and maybe resolve) this difference.

Appendix A Nonlinear models and the Burgers Equation

This appendix shows how two different models of pressure pumping, the Muskat (incompressible flow) model and the weakly nonlinear form of the parabolic (or compressible flow) model, are related to Burgers Equation. Following the notation of the main text the one-dimensional Muskat model is

$$\frac{\partial p_\beta}{\partial t} - \frac{k}{(\eta-\theta)\mu}\left(\frac{\partial p_\beta}{\partial z}\right)^2 = 0 \tag{A1}$$

and the one-dimensional weakly nonlinear form of the parabolic model is

$$\frac{\partial p_\beta}{\partial t} - \frac{k}{(\eta-\theta)\mu}\left(\frac{\partial p_\beta}{\partial z}\right)^2 - P\frac{\partial}{\partial z}\left(\frac{k}{(\eta-\theta)\mu}\frac{\partial p_\beta}{\partial z}\right) = 0 \tag{A2}$$

In terms of the Darcy velocity, $v_p = -k/((\eta-\theta)\mu)(\partial p_\beta/\partial z)$, and the pressure diffusivity, $\kappa = Pk/((\eta-\theta)\mu)$, (A1) can be expressed as

$$\frac{\kappa}{P}\frac{\partial p_\beta}{\partial t} - v_p^2 = 0 \tag{A3}$$

and (A2) as

$$\frac{\kappa}{P}\frac{\partial p_\beta}{\partial t} - v_p^2 + \kappa\frac{\partial v_p}{\partial z} = 0 \tag{A4}$$

Assuming that the temporal and spatial differentiation operators commute, differentiate the last two expressions with respect to z, then employ Darcy's law again (with the further assumption assume that k is not a function of time). This transforms (A1) into the inviscid form of Burgers Equation,

$$\frac{\partial v_p}{\partial t} + 2v_p\frac{\partial v_p}{\partial z} = 0 \tag{A5}$$

and (A2) into a viscid form of Burgers Equation,

$$\frac{\partial v_p}{\partial t} + 2v_p \frac{\partial v_p}{\partial z} - \frac{\partial}{\partial z}\left(\kappa \frac{\partial v_p}{\partial z}\right) = 0 \tag{A6}$$

It may be more appropriate to term Equation (A6) a pseudo-Burgers Equation, because unlike Burgers Equation, the diffusive term $\partial/\partial z\left(\kappa \partial v_p/\partial z\right)$ is much greater in magnitude than the nonlinear term $2v_p \partial v_p/\partial z$ as shown above in the section 2.2.1 of the manuscript. Nevertheless, the standard way of solving viscid Burgers Equation, i.e., the Cole-Hopf transformation (Cole (1951); Hopf (1950)), can also be used to solve (A6) and therefore, (A2) as well. The analytical solution to (A2) is developed as follows:

Define a function $\widehat{p} = \widehat{p}(z,t)$ such that

$$\frac{1}{\widehat{p}}\frac{\partial \widehat{p}}{\partial z} = \frac{1}{P}\frac{\partial p_\beta}{\partial z} \tag{A7}$$

After integrating this last expression with respect to z yields:

$$\ln\left(\widehat{p}(z,t)\right) = \frac{p(z,t)}{P} + \widehat{P}(t) \tag{A8}$$

where $\widehat{P}(t)$ (*dimensionless*) is "the constant of integration", which in this case can be a function of time, t, and is related to the boundary conditions. Next simply apply Equation (A7) to Equation (A2) to obtain

$$\frac{\partial \widehat{p}}{\partial t} - \frac{\partial}{\partial z}\left(\kappa \frac{\partial \widehat{p}}{\partial z}\right) - \widehat{p}\,\widehat{P}'(t) = 0 \tag{A9}$$

where (i) $\widehat{P}'(t) = d\widehat{P}/dt$ is the first derivative of $\widehat{P}$ with respect to t and (ii) (A9) is subject to the boundary condition: $\ln\left(\widehat{p}(0,t)\right) = p(0,t)/P + \widehat{P}(t)$ or $\widehat{p}(0,t) = \widehat{P}_*(t)\exp(p(0,t)/P)$, where $\widehat{P}_*(t) = \exp(\widehat{P}(t))$.

By demonstrating the connection between Burgers Equation and (A1) and (A2) above this Appendix should make numerical and mathematical methods developed for solving Burgers Equation (e.g., Kochina (1961); Platzman (1964); Benton and Platzman (1972); Kadalbajoo and Awasthi (2006); Kurt et al. (2015); Çenesiz et al. (2017); Mohamed (2019)) available for obtaining $p(z,t)$ from either the compressible or incompressible model of pressure pumping in soils.

Appendix B Observed 1 m vertical profiles of ρ_s and k_u at MEF

Table B1. Vertical profile of MEF soil bulk density, ρ_s

Soil Depth (m)	Bulk Density (Mgm^{-3})
0.0 - 0.1	1.20
0.1 - 0.2	1.13
0.2 - 0.3	1.07
0.3 - 0.4	1.02
0.4 - 0.5	1.08
0.5 - 0.6	1.26
0.6 - 0.7	1.48
0.7 - 0.8	1.58
0.8 - 0.9	1.73
0.9 - 1.0	1.63

Table B2. Vertical profile of MEF soil permeability obtained for the top 1 m only. The samples were obtained with a sample tube 0.05 m in length. The vertical sample was obtained with the sample tube inserted vertically into the soil. The horizontal sample was obtained with the sample tube inserted horizontally every 0.05 m starting at 0.025 m.

Soil Depth (m)	Vertical Sample $k(z)$ (10^{-12} m^2)	Horizontal Sample $k(z)$ (10^{-12} m^2)
0.00 - 0.05	11	12
0.05 - 0.10	4.5	13
0.10 - 0.15	1.0	4.9
0.15 - 0.20	5.6	2.9
0.20 - 0.25	3.1	2.4
0.25 - 0.30	1.7	3.0
0.30 - 0.35	1.3	2.8
0.35 - 0.40	1.0	3.7
0.40 - 0.45	1.7	2.4
0.45 - 0.50	1.2	2.6
0.50 - 0.55	2.1	2.1
0.55 - 0.60	2.7	74
0.60 - 0.65	72	8.4
0.65 - 0.70	13	19
0.70 - 0.75	52	12
0.75 - 0.80	25	1.6
0.80 - 0.85	140	120
0.85 - 0.90	120	200
0.90 - 0.95	110	43
0.95 - 1.00	250	28

Appendix C The pressure sensor: calibration and data quality

Soil pressure was measured in a single pit at 0, 10, 20, and 50 cm. The tube inlet for pressure at each of these depths used a stainless steel fitting (Swagelok, Solon, OH) with one end covered with a porous stainless steel mesh, but otherwise open to the soil and the other end connected to a high-precision/limited-range differential pressure transducer (226A Baratron differential capacitance manometer, MKS Instruments, Andover, MA) via Dekoron tubing (0.95 cm O.D., 0.64 cm I.D). The tubing was buried about 0.5 m deep. The other side of the differential pressure transducer was connected to one end of an $\approx$ 1 L stainless steel cylinder used to provide a relatively constant reference pressure, P_{ref}. The other end of the reference cylinder was connected to a solenoid (Skinner valve, model 71215SN2MN00N0, Parker, New Britain, CT) that was periodically opened and closed to refresh the pressure within the reference cylinder whenever the pressure transducer drifted out of range; the cylinder attached to the 50 cm inlet did not have a solenoid valve and instead was plugged. The transducers and reference volumes were placed in a control box that was buried about 1 m under the soil. A CR3000 datalogger (Campbell Scientific), located in a separate enclosure placed on the soil surface, measured and recorded each differential pressure transducer at 1 Hz, and whenever the data for an inlet was out of range (i.e., > 500 Pa or < -500 Pa) the datalogger opened the corresponding solenoid for 2 seconds before closing it. The datalogger also recorded the temperature inside the buried control box with a thermistor (Temp 107 probe, Campbell Scientific) and the temperature within the 50 cm reference cylinder, T_{ref}; instead of a solenoid on this cylinder there was a plug that encased and sealed a platinum resistance thermometer within it (Omega 100-ohm platinum-RTD, model RTD-810, with a Omega signal conditioning module, model OM5IP4-N100-C, Omega Engineering). This methodology pro-

vided differential pressure measurements between the air within the soil and the air within the interior of a rigid reference volume with an arbitrary, but nearly constant, number of molecules (i.e., the pressure captured within the reference cylinder at the time of the last opening/closing of the solenoid valve adjusted for temperature changes within the cylinder as well as leaks, such as and molecular exchange across the pressure sensor's diaphragm).

The original data contained subsets of differential pressure signals whose pressures inside their reference cylinders were arbitrary and varied slowly over time; these signals required stitching to create a coherent dataset for analysis. First, obvious data outliers were identified and removed based on their 5-minute averages or standard deviations. Next, a Bayesian statistical analysis was used to stitch the signals together. The pressure signals between the opening/closing of the solenoid valves were bundled into time blocks, with each time block assigned a Bayesian process parameter describing the cylinder pressure, P_{ref}. The Bayesian statistical analysis predicted the corrected soil pressure, $P_s = P_{s,raw} + P_{ref}$; where the correction term is $P_{ref} = P_{ref,init} + c_{\rho,T} * \rho_{a,ref} * T_{ref} * 287.058 - c_1 t - c_2 t^2 - c_3 t^3$ and t (minutes) is time, $P_{ref,init}$, $c_{\rho,T}$, c_1, c_2, and c_3 are empirical fitting parameters with posterior probability distributions and $\rho_{a,ref}$ is calculated from the ideal gas law using P_a (ambient air pressure, described below) and T_{ref}. Direct measurements of the cylinder temperatures were used, but if missing, the soil temperature at 50 cm depth was substituted. The Bayesian analysis estimates the most likely combination of initial reference cell pressure, temperature drift, and time drift between every purging of the reference cell in order make the four soil pressure signals match each other as well as the match P_a. Finally, P_{ref} was calculated for each five-minute period, and then interpolated to 1 Hz and added to the raw pressure data, $P_{s,raw}$. This methodology, which treats P_a as a standard, yields an average absolute accuracy for the soil pressure sensors of P_a ± 17 Pa, while the difference in precision of the standard deviation between the four soil pressure sensors is ± 1 Pa. Therefore, soil air pressure differences in the vertical can typically be measured within ± 1 Pa while retaining low-frequency trends within each pressure signal.

The ambient pressure is necessary to allow an accurate reconstruction of the soil pressure profiles over time. The goal was to allow the Bayesian analysis to slowly adjust the reference cylinder pressures so that each block of time would accurately reflect the absolute pressure observed at the field site. From 8 July 2009 until 28 September 2012 the absolute ambient pressure was taken from at the National Center for Atmospheric Research (NCAR) Manitou Experimental Forest Observatory, P_{NCAR} (*BEACHON 5 minute ISFS data, not tilt corrected.*, n.d.). After 28 September 2012 there were no absolute ambient pressure measurements recorded at MEF; instead, an adjusted version of the ambient pressure at the Niwot Ridge AmeriFlux site (P_{NR1}) 110 km north-northwest (Blanken et al., 1998) was used. This was done by first developing a relationship between P_{NR1} and P_{NCAR} during the overlap period between 8 July 2009 and 28 September 2012. The P_{NR1} data were LOESS filtered with a 2-day window and then used as an independent variable to predict the NCAR pressure data from the equation $P_{NCAR} = a P_{NR1} + b + c \sin(2\pi t/365.25 + d)$ where a, b, c, and d are empirical fitting parameters and t (days) is time, an independent variable. For both the NCAR and adjusted Niwot Data, the mean value of 76.283 kPa at MEF was removed from the datasets. The Bayesian parameters were adjusted such that the analysis tried to match the four soil pressure sensors with the same precision to each other as P_{NCAR}, but it allowed the matching to P_{NR1} to be less rigorous because this dataset is considered a surrogate for the actual pressures at MEF.

Acknowledgments

The authors wish to thank Dr Al Bedard for his thoughts and insights regarding atmospheric gravity waves, lee waves and infrasound, Dr Ned Patton for his making the NCAR

data available to us, and Dr Shane Mayor for pointing out the UCAR weather data archive at https://www2.mmm.ucar.edu/imagearchive/.

Data Availability Statement

The computer code used in this study was developed using MatLab version 2017b and is publicly available along with any output data at the Forest Service Research Data Archive https://doi.org/10.2737/RDS-2021-XXXX. It is also freely available from the lead author.

References

Albert, M. R. (2002). Effects of snow and firn ventilation on sublimation rates. *Annals of Glaciology*, *35*, 52–56. https://doi.org/10.3189/172756402781817194.

Albert, M. R., & McGilvary, W. R. (1992). Thermal effects due to air flow and vapor transport in dry snow. *Journal of Glaciology*, *38*(129), 273–281. https://doi.org/10.3189/S0022143000003683.

Albert, M. R., & Shultz, E. F. (2002). Snow and firn properties and air–snow transport processes at Summit, Greenland. *Atmospheric Environment*, *36*(15-16), 2789–2797. https://doi.org/10.1016/S1352-2310(02)00119-X.

Bartelt, P., Buser, O., & Sokratov, S. A. (2004). A nonequilibrium treatment of heat and mass transfer in alpine snowcovers. *Cold Regions Science and Technology*, *39*, 219–242. https://doi.org/10.1071/SR9680031.

BEACHON 5 minute ISFS data, not tilt corrected. (n.d.). (NCAR/EOL Data Archive: https://data.eol.ucar.edu/dataset/183867)

Bedard, A. J. (1998). Recent advances in infrasonic and near infrasonic atmospheric sounding and imaging. In *Fourth international workshop on radar polarimetry Nantes, 13–17 July 1998* (pp. 269–). France: Laboratoire systèmes electroniques & informatiques. ISBN 2-909805-09-3.

Bedard, A. J. (2005). Low-frequency atmospheric acoustic energy associated with vortices produced by thunderstorms. *Monthly Weather Review*, *133*(1), 241–263. https://doi.org/10.1175/MWR-2851.1.

Benton, E. R., & Platzman, G. W. (1972). A table of solutions of the one-dimensional Burgers equation. *Quarterly of Applied Mathematics*, *30*(2), 195–212. https://doi.org/10.1090/qam/306736.

Berryman, E. M., Frank, J. M., Massman, W. J., & Ryan, M. G. (2018). Using a Bayesian framework to account for advection in seven years of snowpack CO_2 fluxes in a mortality-impacted subalpine forest. *Agricultural and Forest Meteorology*, *249*, 420–433. https://doi.org/10.1016/j.agrformet.2017.11.004.

Blanken, P. D., Monson, R. K., Burns, S. P., Bowling, D. R., & Turnispeed, A. A. (1998). *AmeriFlux US-NR1 Niwot Ridge Forest (LTER NWT1).* (AmeriFlux Data Archive: https://doi.org/10.17190/AMF/1246088)

Bourret, S. M., Kwicklis, E. M., Miller, T. A., & Stauffer, P. H. (2018). Evaluating the importance of barometric pumping for subsurface gas transport near an underground nuclear test site. *Vadose Zone Journal*, *18*, 180134. https://doi.org/10.2136/vzj2018.07.0134.

Bowling, D. R., & Massman, W. J. (2011). Persistent wind-induced enhancement of diffusive CO_2 fluxes in a mountain forest snowpack. *Journal Geophysical Research*, *116*, G04006. https://doi.org/10.1029/2011JG001722.

Brooks, J. R., Meinzer, F. C., Coulombe, R., & Gregg, J. (2002). Hydraulic redistribution of soil water during summer drought in two contrasting pacific northwest coniferous forests. *Tree Physiology*, *22*, 1107–1117. https://doi.org/10.1093/treephys/22.15-16.1107.

Buckingham, E. (1904). *Contributions to our knowledge of the aeration of soils.* (Bureau of Soils – Bulletin No. 25). Government Printing Office, Washington, D. C.: US Department of Agriculture.

Campbell, G. S., & Norman, J. M. (1998). *An Introduction to Environmental Biophysics.* (Second ed.). New York, NY, USA: Springer-Verlag New York, Inc. (ISBN 0-387-94937-2)

Çenesiz, Y., Baleanu, D., Kurt, A., & Tasbozan, O. (2017). New exact solutions of Burgers type equations with conformable derivative. *Waves in Random and Complex Media*, *27*(1), 103–116. https://doi.org/10.1080/17455030.2016.1205237.

Chen, C., Thomas, D. M., & Green, R. E. (1995). Modeling of radon transport in unsaturated soil. *Journal of Geophysical Research - Solid Earth*, *100*(B8), 15517–15525. https://doi.org/10.1029/2000WR900128.

Christie, D. R. (1989). Long nonlinear waves in the lower atmosphere. *Journal of the Atmospheric Sciences*, *46*(11), 1462–1491. https://doi.org/10.1175/1520-0469(1989)046<1462:LNWITL>2.0.CO;2.

Clarke, G. K. C., Fisher, D. A., & Waddington, E. D. (1987). Wind pumping: A potentially significant heat source in ice sheets. In E. D. Waddington & J. S. Walder (Eds.), *International Association of Hydrological Sciences 170 (Symposium at Vancouver 1987) – The Physical Basis of Ice Sheet Modelling.* (pp. 169–180). IAHS, UKCEH Wallingford, Oxfordshire OX10 8BB, UK: International Association of Hydrological Sciences. ISBN 0-947571-36-1.

Clements, W. E., & Wilkening, M. H. (1974). Atmospheric pressure effects on ^{222}Rn transport across the earth-air interface. *Journal of Geophysical Research*, *79*(33), 5025–5029. https://doi.org/10.1029/JC079i033p05025.

Cole, J. (1951). On a quasi-linear parabolic equation occurring in aerodynamics. *Quarterly of Applied Mathematics*, *9*(3), 225–236. https://www.jstor.org/stable/43633894.

Czepiel, P. M., Shorter, J. H., Mosher, B., Allwine, E., McManus, J. B., Harriss, R. C., et al. (2003). The influence of atmospheric pressure on landfill methane emissions. *Waste Management*, *23*, 593–598. https://doi.org/d10.1016/S0956-053X(03)00103-X.

Depcik, C., & Loya, S. (2012). Dynamically incompressible flow. In S. A. Jones (Ed.), *Advanced methods for practical applications in fluid mechanics* (pp. 71–98). Rijeka, Croatia: InTech. ISBN: 978-953-51-0241-0; Available from: http://www.intechopen.com/books/advanced-methods-for-practical-applications-in-fluidmechanics/dynamically-incompressible-flow.

Doviak, R. J., & Ge, R. (1984). An atmospheric solitary gust observed with a Doppler radar, a tall tower and a surface network. *Journal of the Atmospheric Sciences*, *41*(17), 2559–2573. https://doi.org/10.1175/1520-0469(1984)041<2559:AASGOW>2.0.CO;2.

Drake, S. A., Selker, J. S., & Higgins, C. W. (2019). Pressure-driven vapor exchange with surface snow. *Frontiers in Earth Science*, *7*, 201. https://doi.org/10.3389/feart.2019.00201.

Dubrovin, L. I. (1961). Air currents in the snow and firn layer of Lazarev ice shelf. *Sovetskaia antarkticheskaia ekspeditsiia. Informatsionnyi biulleten.*, *26*, 13-14. English translation in: Soviet Antarctic Expedition, Information Bulletin. Vol. 3, Amsterdam, Elsevier, 1965, p.218–219. https://www.coldregions.org/vufind/Record/139194.

Einaudi, F., Bedard, A. J., & Finnigan, J. J. (1989). A climatology of gravity waves and other coherent disturbances at the Boulder Atmospheric Observatory during MarchApril 1984. *Journal of the Atmospheric Sciences*, *46*(3), 303–329. https://doi.org/10.1175/1520-0469(1989)046<0303:ACOGWA>2.0.CO;2.

Elberling, B., Larsen, F., Christensen, S., & Postma, D. (1998). Gas transport in a confined unsaturated zone during atmospheric pressure cycles. *Water Resources Research*, *34*(11), 2855–2862. https://doi.org/10.1029/98WR02037.

Etiope, G., & Martinelli, G. (2002). Migration of carrier and trace gases in the geosphere: an overview. *Physics of the Earth and Planetary Interiors*, *129*(3-4), 185–204. https://doi.org/10.1016/S0031-9201(01)00292-8.

Faïn, X., Helmig, D., Hueber, J., Obrist, D., & Williams, M. W. (2013). Mercury dynamics in the Rocky Mountain, Colorado, snowpack. *Biogeosciences*, *10*(6), 3793–3807. https://doi:10.5194/bg-10-3793-2013.

Falta, R. W., Javandel, I., Pruess, K., & Witherspoon, P. A. (1989). Density-driven flow of gas in the unsaturated zone due to the evaporation of volatile organic compounds. *Water Resources Research*, *25*(10), 2159–2169. https://doi.org/10.1029/WR025i010p02159.

Finnigan, J. J. (1979). Turbulence in waving wheat I. Mean statistics and honami. *Boundary-Layer Meteorology*, *16*(2), 181–211. https://doi.org/10.1007/BF02350511.

Forde, O. N., Cahill, A. G., Beckie, R. D., & Mayer, K. U. (2019). Barometric-pumping controls fugitive gas emissions from a vadose zone natural gas release. *Scientific Reports*, *9*, 14080. https://doi.org/10.1038/s41598-019-50426-3.

Frank, J. M., & Massman, W. J. (2020). *2008-2014 Soil temperature, thermal conductivity, water content, CO_2, and pressure at the Manitou Experimental Forest, Colorado during the Bio-hydro-atmosphere interactions of Energy, Aerosols, Carbon, H_2O, Organics & Nitrogen (BEACHON) study.* Rocky Mountain Research Station, Fort Collins, Colorado. (Forest Service Research Data Archive: https://doi.org/10.2737/RDS-2020-0061)

Fritts, D. C., & Alexander, M. J. (2003). Gravity wave dynamics and effects in the middle atmosphere. *Reviews of Geophysics*, *41*(1), 1003. https://doi.org/10.1029/2001RG000106.

Fukuda, H. (1955). Air and vapor movement in soil due to wind. *Soil Science*, *79*, 249–256. https://doi.org/10.1097/00010694-195504000-00002.

Goncharov, V. P., & Matveyev, A. K. (1982). Observations of nonlinear waves on an atmospheric inversion. *Izvestiya, Atmospheric and Oceanic Physics*, *18*(1), 61–64. https://www.researchgate.net/publication/259382702.

Gray, J. M. N. T., & Morland, L. W. (1994). A dry snowpack model. *Cold Regions Science and Technology*, *22*, 135–148. https://doi.org/10.1016/0165-232X(94)90025-6.

Grifoll, J., Gastó, J. M., & Cohen, Y. (2005). Non-isothermal soil water transport and evaporation. *Advances in Water Resources*, *28*(11), 1254–1266. https://doi.org/10.1016/j.advwatres.2005.04.008.

Grivet-Talocia, S., Einaudi, F., Clark, W. L., Dennett, R. D., Nastrom, G. D., & VanZandt, T. E. (1999). A 4-yr climatology of pressure disturbances using a barometer network in central Illinois. *Monthly weather review*, *127*(7), 1613–1629. https://doi.org/10.1175/1520-0493(1999)127<1613:AYCOPD>2.0.CO;2.

Hauf, T., Finke, U., Neisser, J., Bull, G., & Stangenberg, J.-G. (1996). A ground-based network for atmospheric pressure fluctuations. *Journal of Atmospheric and Oceanic Technology*, *13*(5), 1001–1023. https://doi.org/10.1175/1520-0426(1996)013<1001:AGBNFA>2.0.CO;2.

Hinch, E. J. (2020). *Think Before You Compute.* Cambridge CB2 8BS, UK: Cambridge University Press. (ISBN 978-1-108-78999-8)

Hinkle, M. E. (1994). Environmental conditions affecting concentrations of He, CO_2, O_2 and N_2 in soil gases. *Applied Geochemistry*, *9*(1), 53–63. https://doi.org/10.1016/0883-2927(94)90052-3.

Hopf, E. (1950). The partial differential equation $u_t + uu_x = \mu u_{xx}$. *Communications on Pure and Applied Mathematics*, *3*(3), 201–230. https://doi:10.1002/cpa.3160030302.

Hu, J., Yang, G., Hegedűs, M., Iwaoka, K., Hosoda, M., & Tokonami, S. (2018). Numerical modeling of the sources and behaviors of ^{222}Rn, ^{220}Rn and their progenies in the indoor environment – A review. *Journal of Environmental Radioactivity*, *189*, 40–47. https://doi.org/10.1016/j.jenvrad.2018.03.006.

Iakovleva, V. S., & Ryzhakova, N. K. (2003). A method for estimating the convective radon transport velocity in soils. *Radiation Measurements*, *36*, 389–391. https://doi.org/10.1016/S1350-4487(03)00157-4.

Ishihara, Y., Shimojima, E., & Harada, H. (1992). Water vapor transfer beneath bare soil where evaporation is influenced by a turbulent surface wind. *Journal of Hydrology*, *131*(1–4), 63–104. https://doi.org/10.1016/0022-1694(92)90213-F.

Jackson, R. D. (1973). Diurnal changes in soil water content during drying. In R. R. Bruce (Ed.), *Field soil water regime* (pp. 37–55). Madison, Wisconsin USA: Soil Science Society of America, Inc. https://doi.org/10.2136/sssaspecpub5.c3.

Jackson, T. J., O'Neill, P., & Swift, C. T. (1997). Passive microwave observation of diurnal surface soil moisture. *IEEE Transactions in Geoscience and Remote Sensing*, *35*, 1210–1222. https://doi.org/10.1109/36.628788.

Jury, W., & Horton, R. (2004). *Soil physics.* (6^{th} ed.). Hoboken, NJ, USA: John Wiley & Sons, Inc. (ISBN: 0-471-05965-X)

Kadalbajoo, M. K., & Awasthi, A. (2006). A numerical method based on Crank-Nicolson scheme for Burgers equation. *Applied Mathematics and Computation*, *182*(2), 1430–1442. https://doi.org/10.1016/j.amc.2006.05.030.

Kidder, R. E. (1957). Unsteady flow of gas through a semi-infinite porous medium. *Journal of Applied Mechanics*, *24*, 329–332. https://doi.org/10.1115/1.4011542.

Kimball, B. A. (1983). Canopy gas exchange: Gas exchange with soil. In H. M. Taylor, W. R. Jordan, & T. R. Sinclair (Eds.), *Limitations to efficient water use in crop production* (pp. 215–226). Madison, Wisconsin USA: ASA, CSSA, and SSSA. https://doi.org/10.2134/1983.limitationstoefficientwateruse.c14.

Koch, S. E., & Siedlarz, L. M. (1999). Mesoscale gravity waves and their environment in the central United States during STORM-FEST. *Monthly Weather Review*, *127*(12), 2854–2879. https://doi.org/10.1175/1520-0493(1999)127<2854:MGWATE>2.0.CO;2.

Kochina, N. N. (1961). Observations of nonlinear waves on an atmospheric inversion. *Journal of Applied Mathematics and Mechanics*, *25*(6), 1597–1607. https://doi.org/10.1016/0021-8928(62)90138-7.

Koppel, L. L., Bosart, L. F., & Keyser, D. (2000). A 25-yr climatology of large-amplitude hourly surface pressure changes over the conterminous United States. *Monthly weather review*, *128*(1), 51–68. https://doi.org/10.1175/1520-0493(2000)128<0051:AYCOLA>2.0.CO;2.

Kraichnan, R. H. (1956). Pressure fluctuations in turbulent flow over a flat plate. *The Journal of The Acoustical Society of America*, *28*(3), 378–390. https://doi.org/10.1121/1.1908336.

Kuang, X., Jiao, J. J., & Li, H. (2013). Review on airflow in unsaturated zones induced by natural forcings. *Water Resources Research*, *49*, 6137–6165. https://doi.org/10.1002/wrcr.20416.

Kurganov, A. (2016). Central schemes: A powerful black-box solver for nonlinear hyperbolic PDEs. In R. Abgrall & C.-W. Shu (Eds.), *Handbook of Numerical Analysis* (pp. 525–548). 1000 AE Amsterdam, The Netherlands: Elsevier B.V. https://doi.org/10.1016/bs.hna.2016.09.008.

Kurt, A., Çenesiz, Y., & Tasbozan, O. (2015). On the solution of Burgers Equation with the new fractional derivative. *Open Physics*, *13*(1), 355–360. https://doi.org/10.1515/phys-2015-0045.

Laemmel, T., Mohr, M., Schack-Kirchner, H., Schindler, D., & Maier, M. (2017). Direct observation of wind-induced pressure-pumping on gas transport in soil. *Soil Science Society of America Journal*, *81*, 770–774. https://doi.org/10.2136/sssaj2017.01.0034n.

Lebeau, M., & Konrad, J.-M. (2009). Natural convection of compressible and incompressible gases in undeformable porous media under cold climate. *Computers and Geotechnics*, *36*, 435–445. https://doi.org/10.1016/j.compgeo.2008.04.005.

Leventhall, G. (2007). What is infrasound? *Progress in Biophysics and Molecular Biology*, *93*(1–3), 130–137. https://doi.org/10.1016/j.pbiomolbio.2006.07.006.

Lewicki, J. L., Evans, W. C., Hilley, G. E., Sorey, M. L., Rogie, J. D., & Brantley, S. L. (2003). Shallow soil CO_2 flow along the San Andreas and Calaveras Faults, California. *Journal of Geophysical Research*, *108*(B4), 2187.

https://doi.org/10.1029/2002JB002141.

Li, J., You, K., Zhan, H., & Huang, G. (2012). Analytical solution to subsurface air pressure in a three-layer unsaturated zone with atmospheric pressure changes. *Transport in Porous Media*, *93*, 461–474. https://doi.org/10.1007/s11242-012-9964-5.

Li, J., Zhan, H., & Huang, G. (2011). Applicability of the linearized governing equation of gas flow in porous media. *Transport in Porous Media*, *87*, 815–834. https://doi.org/10.1007/s11242-011-9720-2.

Li, Y., & Smith, R. B. (2010). Observation and theory of the diurnal continental thermal tide. *Journal of The Atmospheric Sciences*, *76*(9), 2752–2765. https://doi.org/0.1175/2010JAS3384.1.

Luce, C. H., Tonina, D., Gariglio, F., & Applebee, R. (2013). Solutions for the diurnally forced advection-diffusion equation to estimate bulk fluid velocity and diffusivity in streambeds from temperature time series. *Water Resources Research*, *49*, 488–506. https://doi.org/10.1029/2012WR012380.

Maier, M., Schack-Kirchner, H., Aubinet, M., Goffi, S., Longdoz, B., & Parent, F. (2012). Turbulence effect on gas transport in three contrasting forest soils. *Soil Science Society of America Journal*, *76*, 1518–1528. https://doi.org/10.2136/sssaj2011.0376.

Marlton, G., Charlton-Perez, A., Harrison, G., & Lee, C. (2019). Calculating atmospheric gravity wave parameters from infrasound measurements. In A. Le Pichon, E. Blanc, & A. Hauchecorne (Eds.), *Infrasound Monitoring for Atmospheric Studies.* (pp. 701–719). Gewerbestrasse 11, 6330 Cham, Switzerland: Springer Nature Switzerland AG. https://doi.org/10.1007/978-3-319-75140-5_22.

Marty, J., Ponceau, D., & Dalaudier, F. (2010). Using the international monitoring system infrasound network to study gravity waves. *Geophysical Research Letters*, *37*(19), L19802. https://doi.org/10.1029/2010GL044181.

Mass, C. F., Steenburgh, W. J., & Schultz, D. M. (1991). Diurnal surface-pressure variations over the continental United States and the influence of sea level reduction. *Monthly Weather Review*, *119*(12), 2814–2630. https://doi.org/10.1175/1520-0493(1991)119<2814:DSPVOT>2.0.CO;2.

Massman, W. J., Berryman, E., & Frank, J. (2021). *Pressure pumping dramatically impacts soil and snowpack CO2 fluxes and profiles.* AmeriFlux video postcard at https://ameriflux.lbl.gov/, then follow the link https://ameriflux.lbl.gov/pressure-pumping-dramatically-impacts-soil-and-snowpack-co2-fluxes-and-profiles/.

Massman, W. J., Frank, J. M., & Mooney, S. J. (2010). Advancing investigation and modeling of first-order fire effects on soils. *Fire Ecology*, *6*, 36–54. https://doi.org/10.4996/fireecology.0601036.

Massman, W. J., & Lee, X. (2002). Eddy covariance flux corrections and uncertainties in long-term studies of carbon and energy exchanges. *Agricultural and Forest Meteorology*, *113*(1–4), 121–144. https://doi.org/10.1029/2000WR900128.

Massman, W. J., Sommerfeld, R., Mosier, A. R., Zeller, K. F., Hehn, T., & Rochelle, S. (1997). A model investigation of turbulence-driven pressure pumping effects on the rate of diffusion of CO_2, N_2O and CH_4 through layered snowpacks. *Journal of Geophysical Research*, *102*, 18,851–18,863. https://doi.org/10.1029/97JD00844.

Massmann, J., & Ferrier, D. F. (1992). Effects of atmospheric pressures on gas transport in the vadose zone. *Water Resources Research*, *28*(3), 777–791. https://doi.org/10.1029/91WR02766.

Massmann, J. W. (1989). Applying groundwater flow models in vapor extraction system design. *Journal of Environmental Engineering*, *115*, 129–149. https://doi.org/10.1061/(ASCE)0733-9372(1989)115:1(129).

Mohamed, N. A. (2019). Solving one- and two-dimensional unsteady Burgers' equation using fully implicit finite difference schemes. *Arab Journal of Basic and Applied Sciences*, *26*(1), 254–268. https://doi.org/10.1080/25765299.2019.1613746.

Moya, M. R., Sánchez-Cañete, E. P., Vargas, R., López-Ballesteros, A., Oyonarte, C., Kowalski, A. S., et al. (2019). CO_2 dynamics are strongly influenced by low

frequency atmospheric pressure changes in semiarid grasslands. *Journal of Geophysical Research: Biogeosciences*, *124*, 902–917. https://doi.org/10.1029/2018JG004961.

Muskat, M. (1937). *The flow of homogeneous fluids through porous media.* New York, NY, USA: McGraw-Hill Book Co., Inc. (ISBN-13: 978-0934634168)

Nachshon, U., Dragila, M., & Weisbrod, N. (2012). From atmospheric winds to fracture ventilation: Cause and effect. *Journal of Geophysical Research: Biogeosciences*, *117*(G2), G02016. https://doi.org/10.1029/2011JG001898.

Nield, D. A. (1982). Onset of convection in a porous layer saturated by an ideal gas. *International Journal of Heat and Mass Transfer*, *25*(10), 1605–1606. https://doi.org/10.1016/0017-9310(82)90039-4.

Nieveen, J. P., El-Kilani, R. M. M., & Jacobs, A. F. G. (2001). Behaviour of the static pressure around a tussock grasslandforest interface. *Agricultural and Forest Meteorology*, *106*(4), 253–259. https://doi.org/10.1016/S0168-1923(00)00234-3.

Novak, M. D. (2016). Importance of soil heating, liquid water loss, and vapor flow enhancement for evaporation. *Water Resources Research*, *52*, 8023–8038. https://doi.org/10.1002/2016WR01884.

Or, D., & Wraith, J. M. (2000). Comment on 'On water vapor transport in field soils' by Anthony T. Cahill and Marc B. Parlange. *Water Resources Research*, *36*, 3103–3105. https://doi.org/10.1029/2000WR900124.

Ostendorf, D. W., Hinlein, E. S., Lutenegger, A. J., & Kelley, S. P. (2000). Soil gas transport above a jet fuel/solvent spill at Plattsburgh Air Force Base. *Water Resources Research*, *36*(9), 2531–2547. https://doi.org/10.1029/2000WR900128.

Parlange, M. B., Cahill, A. T., Nielsen, D. R., Hopmans, J. W., & Wendroth, O. (1998). Review of heat and water movement in field soils. *Soil & Tillage Research*, *47*, 5–10. https://doi.org/10.1016/S0167-1987(98)00066-X.

Phillips, O. M. (1991). *Flow and reactions in permeable rocks.* New York, NY, USA: Cambridge University Press. (ISBN-13: 978-0521380980, ISBN-10: 0521380987)

Platzman, G. W. (1964). An exact integral of complete spectral equations for unsteady one-dimensional flow. *Tellus*, *16*(4), 422–431. https://doi.org/10.3402/tellusa.v16i4.8995.

Press, W. H., Teukolsky, S. A., Vetterling, W. T., & Flannery, B. P. (2007). *Numerical recipes.* (Third ed.). Cambridge, U.K.: Cambridge University Press. (ISBN 978-0-521-88068-8)

Rains, F. A., Stoy, P. C., Welch, C. M., Montagne, C., & McGlynn, B. L. (2016). A comparison of methods reveals that enhanced diffusion helps explain cold-season soil CO_2 efflux in a lodgepole pine ecosystem. *Cold Regions Science and Technology*, *121*, 16–24. https://doi.org/10.1029/WR025i010p02159.

Ralph, F. M., Neiman, P. J., & Keller, T. L. (1999). Deep-tropospheric gravity waves created by leeside cold fronts. *Journal of the Atmospheric Sciences*, *56*(17), 2986–3009. https://doi.org/10.1175/1520-0469(1999)056< 2986:DTGWCB>2.0.CO;2.

Raspet, R., Abbott, J.-P., Webster, J., Yu, J., Talmadge, C., Alberts, K., et al. (2019). New systems for wind noise reduction for infrasonic measurements. In A. Le Pichon, E. Blanc, & A. Hauchecorne (Eds.), *Infrasound Monitoring for Atmospheric Studies.* (pp. 91–124). Gewerbestrasse 11, 6330 Cham, Switzerland: Springer Nature Switzerland AG. https://doi.org/10.1007/978-3-319-75140-5_3.

Reicosky, D. C., Gesch, R. W., Wagner, S. W., Gilbert, R. A., Wente, C. D., & Morris, D. R. (2008). Tillage and wind effects on soil CO_2 concentrations in muck soils. *Soil & Tillage Research*, *99*, 221–231. https://doi.org/10.1016/j.still.2008.02.006.

Robinson, A. L., Sextro, R. G., & Fisk, W. J. (1997). Soil-gas entry into an experimental basement driven by atmospheric pressure fluctuations – measurements, spectral analysis, and model comparison. *Atmospheric Environment*, *31*, 1477–1485. https://doi.org/10.1016/S1352-2310(96)00304-4.

Rose, C. W. (1968). Water transport in soil with a daily temperature wave I. theory and experiment. *Australian Journal of Soil Research*, *6*, 31–44. https://doi.org/10.1071/SR9680031.

Ruppert, J. H., & Bosart, L. F. (2014). A case study of the interaction of a mesoscale gravity wave with a mesoscale convective system. *Monthly Weather Review*, *142*(4), 1403–1429. https://doi.org/10.1175/MWR-D-13-00274.1.

Rutten, M. M. (2015). *Moisture in the topsoil from large-scale observations to small-scale process understanding.* Unpublished master's thesis, Delft University of Technology. (ISBN: 978-94-6186-434-5)

Sanders, F., & Gyakum, J. R. (1980). Synoptic–Dynamic climatology of the "Bomb". *Monthly Weather Review*, *108*(10), 1589–1606. https://doi.org/10.1175/1520-0493(1980)108<1589:SDCOT>2.0.CO;2.

Scanlon, B. R., Nicot, J. P., & Massmann, J. W. (2002). Soil gas movement in unsaturated systems. In A. W. Warrick (Ed.), *Soil physics companion* (pp. 297–341). Boca Raton, FL 33431: CRC Press LLC. https://doi.org/10.1201/9781420041651.ch8.

Scotter, D. R., & Raats, P. A. C. (1969). Dispersion of water vapor in soil due to turbulence. *Soil Science*, *108*(3), 170–176.

Scotter, D. R., Thurtell, G. W., & Raats, P. A. C. (1967). Note: Dispersion resulting from sinusoidal gas flow in porous materials. *Soil Science*, *104*(4), 206–308.

Shan, C. (1995). Analytical solutions for determining vertical air permeability in unsaturated soils. *Water Resources Research*, *31*(9), 2193–2200. https://doi.org/10.1029/95WR01653.

Shaw, R. H., Paw U, K. T., Zhang, X. J., Gao, W., den Hartog, G., & Neumann, H. H. (1990). Retrieval of turbulent pressure fluctuations at the ground surface beneath a forest. *Boundary-Layer Meteorology*, *50*(3), 319–338. https://doi.org/10.1007/BF00120528.

Shreffler, J. H., & Binkowski, F. S. (1981). Observations of pressure jump lines in the Midwest, 10–12 August 1976. *Monthly Weather Review*, *109*(8), 1713–1725. https://doi.org/10.1175/1520-0493(1981)109<1713:OOPJLI>2.0.CO;2.

Shurpali, N. J., Verma, S. B., Clement, R. J., & Billesbach, D. P. (1993). Seasonal distribution of methane flux in a Minnesota peatland measured by eddy correlation. *Journal of Geophysical Research - Atmospheres*, *98*(D11), 20649–20655. https://doi.org/10.1029/93JD02181.

Sommerfeld, R. A., & Rocchio, J. E. (1993). Permeability measurements on new and equitemperature snow. *Water Resources Research*, *29*(8), 2485–2490. https://doi.org/10.1029/93WR01071.

Thomas, J. W. (1995). *Numerical partial differential equations.* New York, NY, USA: Springer-Verlag. (ISBN 978-0-387-97999-1)

Todd-Brown, K. E. O., Hopkins, F. M., Kivlin, S. N., Talbot, J. M., & Allison, S. D. (2012). A framework for representing microbial decomposition in coupled climate models. *Biogeochemistry*, *109*(1), 19–33. https://doi.org/10.1007/s10533-011-9635-6.

Waddington, E. D., Cunningham, J., & Harder, S. L. (1995). The effects of snow ventilation on chemical concentrations. In E. W. Wolff & R. C. Bales (Eds.), *Chemical exchange between the atmosphere and polar snow* (pp. 403–451). Berlin Heidelberg: Springer-Verlag. https://doi.org/10.1007/978-3-642-61171-1_18.

Wang, H., & Takle, E. S. (1995). A numerical simulation of boundary-layer flows near shelterbelts. *Boundary-Layer Meteorology*, *75*(1-2), 141–173. https://doi.org/10.1016/0883-2927(94)90052-3.

Wang, X., Lei, H., Feng, L., Zhu, J., Li, Z., & Jiang, Z. (2020). Analysis of the characteristics of gravity waves during a local rainstorm event in Foshan, China. *Atmospheric and Oceanic Science Letters*, *13*(2), 163–170. https://doi.org/10.1080/16742834.2020.1719567.

Weisbrod, N., Dragila, M. I., Nachshon, U., & Pillersdorf, M. (2009). Falling through the cracks: The role of fractures in Earth-atmosphere gas exchange. *Geophysical*

Research Letters, *36*(2), L02401. https://doi.org/10.1029/2008GL036096.

Xu, L., Lin, X., Amen, J., Welding, K., & McDermitt, D. (2014). Impact of changes in barometric pressure on landfill methane emission. *Global Biogeochemical Cycles*, *28*, 79–95. https://doi.org/10.1002/2013GB004571.

Yu, J., Raspet, R., Webster, J., & Abbott, J. (2011). Wind noise measured at the ground surface. *The Journal of The Acoustical Society of America*, *129*(2), 622–632. https://doi.org/10.1121/1.3531809.